A multiscale characterisation of the Early Jurassic upper member of the McCarthy Formation, Southcentral Alaska

Y. Heinhuis

26-05-2023

Supervised by:

Dr. J.P. Trabucho-Alexandre

Dr. A.H. Caruthers

Universiteit Utrecht

Comparative SEDIMENTOLOGY Utrecht

Acknowledgement

Contents

List of figures

List of tables

Abstract

Ocean circulation, reflected in bottom current strength, is an essential factor in determining the global climate. Therefore, the deposits of ancient bottom currents are of great paleoclimatic importance. The sparse evidence of bottom currents in the Mesozoic has been linked to sluggish ocean circulation. Arguably, the sparse evidence is caused by the fact that recognition of ancient bottom current deposits is notoriously difficult, especially in mixed depositional systems. In this study, I present a multiscale characterisation of the upper member of the McCarthy Formation, an Early Jurassic record of bottom current deposition. The upper member of the McCarthy Formation has been interpreted as a glass ramp, deposited in the tropical Panthalassa Ocean, now exposed in the Wrangell Mountains, Southcentral Alaska. I studied the upper member along two sections near the Grotto Creek and subdivided it into a cliff succession and a slope succession. I interpreted the cliff succession as the record of a turbidity current–dominated mixed system and the slope succession as the record of a bottom current–dominated mixed system.

The turbidity current–dominated succession is inferred from the lobe architecture of the cliff succession, as well as the dominant presence of spiculitic sandy mudstone, indicative of down-ramp transport of grains by turbidity currents. The shift towards a bottom current–dominated mixed system is inferred from the dominant presence of laminated and bioturbated siliceous mudstones as well as the presence of bigradational bedding, interpreted as contourites, reworked turbidites, and hemipelagites, indicative of a laterally migrating sediment drift. The shift towards a bottom current–dominated mixed system is dominantly caused by a decrease in turbiditic activity rather than an increase in bottom current speeds. This is evident from an absence of sponge spicules, and medium and large scale sedimentary structures in the cliff succession, as well as paleocurrent speed reconstructions.

Bottom current speeds ranging from 9–51 cm/s have been reconstructed from grain size distributions obtained from the siliceous mudstone of the upper member of the McCarthy Formation. Evidence of bottom currents suggests that circulation in the Panthalassa Ocean during the hothouse conditions of the Early Jurassic was likely more vigorous than previously thought.

Introduction

Bottom currents are an element of ocean circulation, which in turn is responsible for dispersing massive amounts of heat and therefore is directly linked to global climate (Rahmstorf, 2002). Extinction events throughout geological history have been associated to changes in global ocean circulation, causing widespread stratification and anoxia (Isozaki, 1997; Kiehl and Shields, 2005; Saunders and Reichow, 2009; Dera and Donnadieu, 2012; Ruvalcaba Baroni et al., 2018). Modern day ocean circulation can be measured, but reconstructing ocean circulation throughout Earth's history requires the study of the deposits that ancient bottom current left in the rock record. The deposits of ancient bottom currents therefore are of great paleoclimatic importance (Viana and Rebesco, 2007; Bahr et al., 2014; Smillie and Stow, 2017; Alonso et al., 2021). Few records of ancient bottom currents from the Mesozoic have been identified (Georgiev and Botoucharov, 2007; Barnolas and Llave, 2012; Frébourg et al., 2013; Creaser et al., 2017; Sansom, 2018; Thiéblemont et al., 2020; Rodrigues et al., 2021; Paz et al., 2022). This sparse evidence of bottom currents has been linked to slow ocean circulation during hothouse climates, which is also reflected by oceanographic models of the Panthalassa Ocean (Kutzbach et al., 1990; Winguth et al., 2002). Instead of slow ocean circulation, the sparse evidence of bottom currents may be attributed to the fact that ancient bottom current deposits are notoriously hard to identify because they interact with other processes, such as hyperpycnal flows, pelagic, and hemipelagic settling, incorporating fine-grained material from these processes in their deposits (Stow and Faugères, 2008). A common example is when bottom currents rework turbiditic deposits, resulting in a mixed facies (Stow and Smillie, 2020; Cauxeiro et al., 2020). In order to identify bottom currents in the rock record accurately, the study of their deposits on multiple scales is necessary (Hüneke and Stow, 2008, tbl. 17.1). Small scale is used to assess whether or not a distinction can be made between turbidite and contourite facies. Large scale is used to study the architecture of a contourite drift. However, the characterisation of the large-scale architecture is often problematic since study of the large-scale features requires large, well-exposed outcrops.

In this project, I studied the upper member of the McCarthy Formation, an Early Jurassic record of bottom current deposition. The upper member of the McCarthy Formation has been interpreted as a glass ramp, deposited in the tropical Panthalassa ocean (Caruthers et al., 2022; Veenma et al., 2022). The upper member of the McCarthy Formation is three dimensionally

exposed in large outcrops on Chitistone Mountain, near the hamlet of McCarthy, in Southcentral Alaska. This enables the study of the large-scale architecture of the depositional system, and thus an accurate identification of bottom currents in the rock record. I characterised the upper member of the McCarthy Formation on three length scales and obtained grain size distributions of the siliceous mudstones to quantify paleocurrent speeds.

I hypothesise that the upper member of the McCarthy Formation represents a shift from a turbidite-dominated mixed system to a bottom current–dominated mixed system, following the classification of Rodrigues et al. (2022). This adds the McCarthy Formation to the few known records of bottom current activity in the Mesozoic and indicates that ocean circulation in the Panthalassa Ocean during the Hettangian may have been more vigorous than previously thought. Improved recognition of bottom current deposits, especially in mixed systems, may lead to the interpretation of more vigorous ocean circulation during other hothouse periods in Earth's history as well.

Geological background

Southcentral Alaska is a region whose geology is dominated by the accretion of three composite terranes, separated by major fault systems. In the north, the Wrangellia composite terrane borders the Yukon-Tanana composite terrane along the Denali fault and, in the south, it borders the Southern Margin composite terrane along the Border Ranges fault (Nokleberg et al., 1994). The Wrangellia composite terrane, also called the AWP terrane, consists of the Alexander, Wrangellia, and Peninsular tectonostratigraphic terranes. Unlike the other two terranes, which are continuous, Wrangellia consists of a northern (Alaska) and a southern block (British Colombia) (Jones et al., 1977). On the northern block of Wrangellia, the strata of the McCarthy Formation were deposited in the roughly WNW-ESE striking Wrangell Mountains Basin during the Late Triassic to Early Jurassic (Trop et al., 2002). During this time period, Wrangellia was located in the tropical regions of the Panthalassa Ocean. The exact paleolatitude is debated but there is a general consensus, based on fossil content and paleomagnetic data, that Wrangellia was situated within 20° north of the equator (Jones et al., 1977; Hillhouse and Coe, 1994; Butler et al., 1997; Caruthers and Stanley, 2008). Paleobiogeographic data suggest that, by Early Jurassic time, the Wrangellia terrane had moved northward by ~25°–30° (Silberling et al., 1997; Aberhan, 1998). During the Late

Cretaceous to early Paleogene (~100–55 Ma), Wrangellia accreted onto the western margin of Laurasia (Csejtey Jr. et al., 1982; McClelland et al., 1992; Hillhouse and Coe, 1994).

The Triassic of the northern block of Wrangellia consists mainly of Nikolai Greenstone, which near McCarthy is a 3,000 m thick basalt deposit, emplaced during a single phase of subaerial tholeiitic volcanism 230–225 million years ago (Greene et al., 2010). The existence of this basaltic high in the Panthalassa Ocean allowed for the formation of a carbonate platform in relatively shallow water on top of the basement rock (Armstrong et al., 1969; MacKevett, 1970; Jones et al., 1977). The Triassic–Jurassic sedimentary strata that were deposited on top of the Nikolai Greenstone are (from bottom to top) (1) the Chitistone Limestone Formation; (2) the Nizina Limestone Formation; (3) the McCarthy Formation; and (4) the Lubbe Creek Formation (figure 1). The Chitistone Limestone and the Nizina Limestone were deposited from the Carnian to the late Norian. The lower Chitistone Limestone has been interpreted as the record of a supratidal to intertidal environment, whereas the upper Chitistone Limestone and the Nizina Limestone have been interpreted as the record of a shallow-water shelf environment (Armstrong et al., 1969). Disconformably overlying the Nizina Limestone, ~540 m of siliceous mudstones of the McCarthy Formation were deposited from the Norian until the Sinemurian (or Pliensbachian). The transition from the Nizina Limestone to the McCarthy Formation is thought to represent rapid drowning of the carbonate shelf, as a result of post-volcanic thermal subsidence of the basaltic high (MacKevett, 1970; Trop et al., 2002; Witmer, 2007).

MacKevett (1970) divided the McCarthy Formation into a lower and an upper member. The lower member of the McCarthy Formation has been interpreted as the Norian to Rhaetian record of the distal environments of a siliceous carbonate ramp, a term first introduced by Ahr (1973) after failed attempts to fit some carbonate facies to existing shelf models. The term carbonate ramp was refined as it became more widely accepted (Read, 1982, 1985). A carbonate ramp is now known as a sedimentary system that has a low gradient depositional slope, where dominant seafloor sediments are of carbonate mineralogy, from a shallow water shoreline or lagoon to a basin floor (Burchette and Wright, 1992; Wright and Burchette, 1998). The upper member of the McCarthy Formation has been interpreted as the Hettangian to Sinemurian record of a spiculitic glass ramp (Veenma et al., 2022). A glass ramp has a similar architecture to a carbonate ramp but the dominant sediment are siliceous skeletal grains, such as spicules (Gates et al., 2004;

Ritterbush, 2019). This evolution from carbonate to glass ramp in the McCarthy Formation represents a recovery phase of silica-secreting organisms on the Wrangellia terrane after the Triassic–Jurassic mass extinction (Veenma et al., 2022). The depositional dip of the ramp has been interpreted to be towards the west-southwest (Veenma et al., 2022). Isopach maps of the Chitistone, Nizina, and McCarthy formations, as well as thickness observations of the formations by Martin (1916), illustrate this ramp orientation. This interpretation is in contrast to that of Trop et al. (2002), who suggested that the ramp dipped towards the northeast.

The McCarthy Formation is overlain by the Pliensbachian–Toarcian shallow-marine Lubbe Creek Formation. This succession has been suggested to represent a forced regression (Veenma et al., 2022). The Lower Jurassic succession ends with a disconformity representing a hiatus of 10–15 Ma (Trop et al., 2002).

Materials and methods

The Grotto Creek section

The subject of this study is the Hettangian to Sinemurian upper member of the McCarthy Formation, exposed on the slopes of the Chitistone Mountain, ~25 km east-northeast of McCarthy (Wrangell Mountains, Southcentral Alaska). The succession of the upper member is best accessed along an unnamed tributary of Grotto Creek, itself a tributary of the Chitistone River. The Grotto Creek section was originally described by Witmer (2007). Recently, Caruthers et al. (2022) revisited the section and presented biostratigraphic and chemostratigraphic data, as well as U-Pb radiometric age data on bentonites from the Triassic–Jurassic interval. Veenma et al. (2022) presented a facies analysis and a paleoenvironmental interpretation of the uppermost Norian to lowermost Hettangian interval. The 0 m datum of the Grotto Creek section was placed just below the Norian–Rhaetian boundary at the base of an easily recognizable ~5 cm thick bentonite (Veenma et al., 2022). Following MacKevett's (1963) definition of the upper member, the base of the upper member was placed at 58.8 m (Veenma et al. 2022). We estimate the top of the upper member at 430 m, based on thickness measurements by Witmer (2007). Consequently, the upper member of the McCarthy Formation is ~370 m thick (figure 1).

Fieldwork

The upper member of the McCarthy Formation was studied along two sections. One section was visited on foot along the unnamed tributary of the Grotto Creek that ran past our camp site, hereafter named the camp section. The other section is inaccessible on foot and was therefore studied from a piper cub airplane, hereafter named the plane section (figure 2). In both sections, at a height of ~175 m, a vertical separation of the upper member is made based on weathering of the rocks. The lower subdivision is named the cliff succession and the upper subdivision is named the slope succession. We visited the exposures of the upper member in July 2022. We described, measured, and sampled the upper member of the McCarthy Formation on three length scales, described below. We took photographs with a Nikon D3400 Camera with an 18–55 mm lens. We measured the attitude of beds with a compass declination of 17.5°E. Coordinates are given in UTM map datum NAD83.

Decametre (~10–100 m) scale

I took photographs of the upper member from a Piper Cub airplane. The airplane flew along the plane section, where the upper member is exposed in large three-dimensional outcrops. The aerial photographs of the upper member were used to construct panorama panels of the stratigraphy between ~80–180 m. They were used to study the architecture of the upper member, the spatial distribution of large scale (10–17 m thick) low angle cross-stratification (Heinhuis, 2020), and the lateral continuity of an erosional surface, separating the cliff succession and the slope succession.

Metre (~1 m) scale

We studied the rocks of the upper member in the field along the camp section. I took outcrop photographs of the upper member. Study in the field and of outcrop photographs focused on sigmoidal features in the cliff succession and distinct bedding patterns in the slope succession. Between the stratigraphic height of 124 m and 131 m (base at 07V 423,197 m E; 6,820,426 m N), we measured the strike/dip of 8 sets of sigmoidal features (~30 cm thick) and of the corresponding S_0 (figure 3). In sets with bidirectional features, we obtained measurements in both directions. Eleven measurements of sigmoidal features were obtained, as well as three S_0 measurements. I used the average of the three S_0 measurements to rotate the sigmoidal features in a stereonet so that the S_0 is horizontal. The resulting dip direction of the sigmoidal features indicates paleocurrent directions (see discussion). Between the stratigraphic height of 175 m and 232 m (Top at

07V 423,260 m E; 6,820,733 m N), we made observations on the bedding of the slope succession. We focused on changes in lithology, grading in the texture, and sedimentary structures in the rock.

Centimetre (~1 cm) scale

During the field seasons of 2019 and 2022, 91 samples of the upper member were collected, covering 192.2 m of stratigraphy. Sampling resolution was limited by the exposure of the rocks in the Grotto Creek section, affected by debris and snow cover, resulting in less dense sampling above the stratigraphic height of 180 m. To study the properties of beds with sigmoidal features, we sampled two such beds (126 and 129 m). We sampled two additional beds (144.5 and 145 m) without such features to enable comparison (sample location at 07V 423,197 m E; 6,820,426 m N) (table 1).

Table 1: Collected samples of the upper member of the McCarthy Formation. Heights are relative to 0 datum of composite section. Unused samples are either duplicates or not taken in situ. Stratigraphic thickness covered by samples is 192.2 m.

Height [m]	Sample code	Year collected	Used in this study
	n = 91		n = 83
60	32.28A	2019	x
60.1	32.28B	2019	
60.34	32,62	2019	
65.3	GC69	2019	x
70.73	19GC43	2019	x
72.73	19GC45	2019	x
74.73	19GC47	2019	x
77.73	19GC50	2019	x
80.73	19GC53	2019	x
84.73	19GC57	2019	x
87.73	19GC60	2019	x
88.73	19GC61	2019	x
89.73	19GC62	2019	x
90.73	19GC63	2019	x
91.73	19GC64	2019	x
92.73	19GC65	2019	x
93.73	19GC66	2019	x
96.73	19GC69	2019	x
98.73	19GC71	2019	x
100.73	19GC73	2019	x
101.73	19GC74	2019	x
102.73	19GC75	2019	x
103.73	19GC76	2019	x

104.73	19GC77	2019	x	
105.73	19GC78	2019	x	
106.73	19GC79	2019	x	
109.73	19GC82	2019	x	
112.73	19GC85	2019	x	
114.73	19GC87	2019	x	
117.73	19GC90	2019	x	
118.73	19GC91	2019	x	
119.73	19GC92	2019	x	
120.73	19GC93	2019	x	
121.73	19GC94	2019	x	
122.73	19GC95	2019	x	
123.73	19GC96	2019	x	
124.73	19GC97	2019	x	
125.73	19GC98	2019	x	
126	126	2022	x	
126.73	19GC99	2019	x	
127.73	19GC100	2019	x	
128.73	19GC101	2019	x	
129	129	2022	x	
131.73	19GC104	2019	x	
134.73	19GC107	2019	x	
136.73	19GC109	2019	x	
139.73	19GC112	2019	x	
142.73	19GC115	2019	x	
144.5	144,5	2022	x	
145	145	2022	x	
145.73	19GC118	2019	x	
148.73	19GC121	2019	x	
150.73	19GC123	2019	x	
151.73	19GC124	2019	x	
152.48	124,76	2019	x	
152.58	124,86	2019	x	
152.73	19GC125	2019	x	
153.73	19GC126	2019	x	
154.73	19GC127	2019	x	
155.73	19GC128	2019	x	
156.73	19GC129	2019	x	
157.73	19GC130	2019	x	
158.73	19GC131	2019	x	
158.93	131,2	2019	x	
160.73	19GC133	2019	x	
161.73	19GC134	2019	x	
169.73	19GC142	2019	x	
173.73	19GC146	2019	x	
179.73	19GC152	2019	x	

180.73	19GC153	2019	x	
181.73	19GC154	2019	x	
185.73	19GC158	2019	x	
186.73	19GC159	2019	x	
187.73	19GC160	2019	x	
188.73	19GC161	2019	x	
190.73	19GC163	2019	x	
201.43	173,7	2019	x	
202.22	174,5	2019	x	
226.88	199,15	2019	x	
227.47	199,75	2019	x	
236.78	209,05	2019	x	
236.87	209,15	2019	x	
243.08	215,36	2019	x	
246.33	218,6	2019	x	
252.2	226,48	2019		
252.2	226.48.2	2019	x	
NA	ULM-D1	2019		
NA	ULM-D2	2019		
NA	ULM-E2	2019		
NA	ULM-E(1)	2019		
NA	ULM-E(2)	2019		

Analytical work

Eighty-three rock samples were used to produce ~20 μm thick thin sections.
Scans of the thin sections were made using a Leica M165c
stereomicroscope. The study of the thin sections and of the scans focused on
microfacies (including composition and micro-scale sedimentary structures)
and texture. Thirty-eight of the thin sections of the upper member of the
McCarthy Formation were used by Veenma et al. (2022, fig. 4). They
proposed 4 microfacies. For comparative reasons with prior studies, the
microfacies proposed by Veenma et al. (2022) have been adopted in this
study (table 2). The microfacies present in the upper member are MF1a,
MF1b, MF1c, MF4, MF5, MF6a and MF6b. A more detailed description of
the microfacies is given by Veenma et al. (2022, tbl. 3). By examination of
the thin sections under a petrographic microscope, all 83 samples were
assigned to a micro-facies. The textural study of the rock samples was
hindered by the silica cement in the samples. Despite chemical pretreatment,
few samples disaggregated and could be measured using laser particle
analysis (Veenma et al., 2022). Therefore, we used image analysis on thin
sections for grain size analysis. The obtained grain size distributions for the

samples were used to estimate paleocurrent speeds. The grain size analysis and the paleocurrent estimation is described below in further detail.

Table 2: Microfacies for the McCarthy Formation, adopted from Veenma et al. (2022).

Microfacies	Description
MF1a	Fine mudstone with basal silt laminae
MF1b	Fine mudstone with parallel laminae
MF1c	Burrowed fine mudstone
MF4	Calcisphere packstone
MF5	Spiculitic sandy mudstone
MF6a	Laminated sandy mudstone
MF6b	Sandy mudstone with wavy laminae

Image analysis

To determine the grain size distribution of the samples, I used ImageJ, an image analysis software by Fiji, on 25× magnification micrographs, produced by a Zeiss axiocam 305 colour. These micrographs showed the best preparatory results compared to Leica scans, and 50× magnification micrographs (see supplementary materials). The micrographs with 25 times magnification were processed in ImageJ as follows: First, a representative area of the thin section was selected, by examining the thin section for heterogeneity. Subsequently, the micrograph is taken, taking care to avoid stained parts of the thin sections, as this may reduce contrast between grains and matrix (see supplementary materials). The resulting image was converted to 8-bit, necessary to apply further functions in ImageJ. The subtract background function was used to remove the effect of an uneven background, caused by uneven lighting, bioturbation and cementation. This uses a so-called rolling ball algorithm, which functions as follows: "A local background value is determined for every pixel by averaging over a very large ball around the pixel. This value is hereafter subtracted from the original image, hopefully removing large spatial variations of the background intensities" (ImageJ, 2023). The radius of the rolling ball was set to the size of the largest particle not part of the background. The resulting image has better distinguishable grains that are enhanced further using the enhance contrast function. We assumed that the thickness (~ 20 μm) of the thin sections causes grains finer than 20 μm to show up as a dark matrix and the grains coarser than 20 μm to show up as light spots (see supplementary materials). Hence, a brightness threshold was applied to the image, differentiating between dark matrix and light grains, producing a binary image of the grains. Some samples contain dark grains. To account

for these, the process was repeated with a reversed brightness threshold, differentiating between dark grains and light background. In samples with both light and dark grains, the binary images were spliced using the image calculator function. The resulting binary image after the application of the brightness threshold included all grains, both light and dark. In some cases, grain edge detection by ImageJ is not sufficient, leading to clustering of grains. This is resolved by manually disconnecting the clusters by drawing lines along the grain boundaries with the pen tool in ImageJ. Positions of the grain boundaries are determined visually by comparing the binary image with the original micrograph. This step was found to have strong impact on the grain size distribution (see supplementary materials). Grains that are cut off by the edge of the image are deleted from the binary image, since their size is undefinable. This step has little impact on the grain size distribution due to the small area that is occupied by these partial grains (see supplementary materials). Finally, the analyse particles function in ImageJ was used to measure the area of all individual grains (figure 4). A particle size filter was applied to reduce noise, excluding all grains with an area smaller than 314 μm^2, which corresponds to the area of grains with a nominal diameter of 20 μm.

Grain size distribution

The ImageJ output gives an area in μm^2 for each measured grain. From the area, the nominal diameter was calculated. Conventionally, the nominal diameter is the diameter of a spherical grain with the same volume as the measured grain. In this study, the area of a grain, measured in a 2D image is considered a proxy for the volume. Thus here, the nominal diameter is the diameter of a circular grain with an area that is equal to the measured grain. The nominal diameter was used to bin the grain size data following a modified version of the Wentworth scale (Wentworth, 1933). The modification is the result of the observation limit at 20 μm. Since there are no data in the clay fraction and truncated data in the finer silt fraction, we defined the operational bins of fine silt (20–31.125 μm) and coarse silt (31.125–62.5 μm). The Wentworth bins in the sand fraction are unaltered. In this study, the coarsest grain is medium sand. Thus, the grains are binned in a total of 5 bins. Binning was carried out automatically using a MATLAB script (Appendix A). After binning of the grains, the total area of the micrograph and the combined area of the grains in a bin, were used to calculate the area percentage of the five bins. The remaining area, calculated by subtracting the sum of the total area of each bin from the total area of the

micrograph, is a combination of mud, cement and pore space. This is assigned to the matrix bin (0–20 μm).

Using GRADISTAT (Blott and Pye, 2001), I obtained the mean, the median, and the skewness of the distributions from the area percentage data of the 20–500 μm fraction of the samples. The GRADISTAT software includes several methods for statistics calculation. We used the geometric (based on a log-normal distribution with metric size values) Folk and Ward graphical method (1957). This method suits our sparse dataset, because it uses linear interpolation between adjacent known points on a cumulative percentage curve. Metric size values are used because metric values are also used to calculate paleocurrent speeds, thus avoiding the need for conversion between metric values and the phi scale. GRADISTAT does not allow for calculation of the D99 and is less accurate when calculating the D90, because it ignores the outer 5% of the data (Blott and Pye, 2001). Therefore, I wrote a MATLAB script to calculate the D90 and the D99 from the ImageJ grain size data (Appendix A).

Paleocurrent speed reconstruction

I used the sortable silt (SS) proxy of McCave et al. (2017), and the sortable silt and very fine sand (SSFS) proxy of Wu et al. (2021) to estimate paleocurrent velocities throughout the upper member of the McCarthy Formation. The proxies function based on an empiric relationship between the mean of a certain grain size fraction and the depositional flow speed. The proxy of Wu et al. (2021) was incorporated because of the relationship between the sortable silt and the very fine sand (see supplementary materials).

Originally, the lower limit of the used grain size fraction in both proxies is 10 μm. This however conflicts with the lower observation limit of 20 μm, which is the result of the thin section thickness. Therefore, the definitions of SS and SSFS were changed from $10 - 62.5$ μm to $20 - 62.5$ μm, and from $10 - 125$ μm to $20 - 125$ μm respectively.

McCave et al. established a calibration curve with the function:

$$U = 1.36 \times mean\ SS$$

Where U is the flow velocity in cm/s, and mean SS is the mean of the sortable silt fraction, which is defined here as the grains between 20 and 62.5 μm.

Wu et al. established a calibration curve with the function:

$$V = \frac{mean\ SSFS\ -\ 4.61}{2.76}$$

Where V is the flow velocity in cm/s, and the mean SSFS is the mean of the sortable silt plus the very fine sand fraction, which is defined here as grains between 20 and 125 μm.

Results

The 192.2 m thick studied section of the upper member of the McCarthy Formation is subdivided into two subsections, that are separated based on differences in weathering. The lower subsection is 120 m thick, cliff forming, and is hereafter named the cliff succession. The upper subsection is 73.4 m thick, slope forming, and is hereafter named the slope succession. The transition between the two subsections at a stratigraphic height of ~175 m above the 0 m datum is abrupt. We infer an erosional surface at the abrupt transition, due to its undulating nature, sometimes truncating the bedding of the cliff succession (figure 5, figure 6). The subdivision of the upper member into two subsections at this height corresponds to subdivisions made by other authors, such as the informal upper limestone and upper shale members by Witmer (2007), and the division into two facies associations by Veenma et al. (2022).

Table 3: Orientation measurements of horizontal bedding planes (124, 126.2, 127) and diagonal bedding planes (144, 146). The average of the horizontal bedding planes is used to rotate 144 and 146, using a stereonet, so that the average is horizontal, producing 144' and 146'.

Stratigraphic height [m]	Strike [°N]	Dip [°]
124	283	6 N
126.2	300	8 N
127	292	4 N
Average	291	6 N
144	204	2 W
146	196	9 W
144'	130	6 SW
146'	164	11 W

The cliff succession is medium to thick bedded, following the definition by Campbell (1967). The beds are sub horizontally oriented. The cliff succession is well exposed on the sides of the mountain and can be followed laterally for ~2 km. The (sub)horizontal medium to thick beds are organized in prominent protruding bundles of approximately 10 meters thick, alternated with sloping weathered material (figure 5). Below 90 m, between 105–121 m, and above 140 m, three sets of large scale low angle cross stratification with a height of 10–17 m and a corrected dip angle of 6–8° towards the southwest are present in the succession (figure 5, figure 6)(Heinhuis, 2020). Aerial observation of outcrops of the upper member revealed that the upper set of low angle cross-stratification is exposed in two outcrops 2.3 km from each other in which the bedding orientation is the same (figure 7). The cross stratification is interpreted as foresets of sediment waves, which is discussed in more detail below under "Interpretation of sedimentary structures" at the end of the results section. Both the horizontal bedding and the cross-stratification contain folded beds that are interpreted as soft sediment deformation by slumping (figure 8). The lithology of the cliff forming member has been described as dark spiculitic cherts with buff-coloured carbonate concretionary horizons (Veenma et al., 2022). The concretions making up the horizons are ~30 cm thick and ~60 cm wide, varying in thickness in parts of the succession with large scale low angle cross-stratification. Here, the concretions are ~8 cm tall and 10–20 cm wide. The beds in between the concretions are thinner and grey to black coloured (figure 9). Between stratigraphic height of 126 – 132 m, 8 sets of sigmoidal structures that downlap on the bed below are present in the concretionary horizons (figure 10, figure 11, figure 12, figure 13, figure 14, figure 15, figure 16). The beds containing the structures are ~30 cm thick. At the height of 124 m, 128.5 m, and 130.5 m, bidirectional features are observed within one set (figure 10, figure 15, figure 16), whereas in the other sets, the features are oriented in only one direction. The measured orientations have a bimodal distribution of dip directions to the NE and SW (figure 17, figure 18. The sigmoidal features are interpreted as cross-bedding, which is discussed in more detail below under "Interpretation of sedimentary structures" at the end of the results section.

The slope succession is mostly very thin to thin bedded. Every 1–10 m, medium to thick beds intercalate the very thin to thin bedding (figure 19). The beds are subhorizontal. The slope succession is exposed on the mountain ridges, sometimes capped off by the Lubbe Creek Formation. The lithology of the slope forming succession has been described by Veenma et al. (2022) as fissile dark olive to black coloured siliceous mudstones. The

intercalating medium to thick beds are laminated calcareous chert (Veenma et al., 2022). The thicker beds are characterized by bigradational grading, a vertical transition from reverse to normal grading within the bed. This change is mimicked by the coloration of the bed, changing from dark grey at the base and top of the bed to buff-coloured in the middle (figure 20). Parallel thin lamination with alternating colour (buff and dark grey) and texture is present towards the top and bottom of the bed. The middle of the bed is massive. Some beds contain chert nodules (1-2 cm thick, 5-15 cm wide), focused along horizons in the coarse centre of the bed (figure 21). Some horizons between medium to thick beds are undulating resembling an erosional base. Asymmetrical ripples in the beds are interpreted as current ripples (figure 22).

Table 4: Orientation measurements of the sigmoidal features (n = 11). Strike and dip direction are measured in degrees from north. Dip is measured in degrees from horizontal.

Stratigraphic height [m]	Strike [°N]	Dip [°]
124	326.3	31.7 SW
124	326.6	33 NE
126.2	314.6	19.9 NE
127	336.1	26.9 SW
128.5	337.3	25.7 SW
128.5	9.1	13.7 E
129.5	317.7	31.2 SW
130	308.9	20.2 SW
130.5	321.4	16.7 NE
130.5	288.5	32 SW
131	308.2	24.2 NE

Microfacies

Eighty-three thin sections of the upper member of the McCarthy Formation were assigned to the established microfacies (table 2, figure 31). Representative micrographs were selected (figure 24, figure 25, figure 26, figure 27, figure 28, figure 29, figure 30), and their distribution throughout the stratigraphy and interpretation are discussed below.

Between the stratigraphic height of 60 m and 102.73 m, the upper member is an alternation of microfacies MF1c and MF4 with 2 occurrences of MF5 at height 60 m and 98.73 m, and one occurrence of MF1a at height 65.3 m. Bioturbated mudstone and calcisphere packstone are interpreted as

dominant hemipelagic sedimentation. The basal silt laminae in the fine mudstone at height 65.3 m is interpreted as winnowing, likely by bottom currents. The spiculitic sandy mudstone at 60 and 98.73 m is interpreted as influxes of organic debris coming from shallower parts of the glass ramp, likely transported in turbidity currents. Between the stratigraphic height of 103.73 m and 161.3 m, the upper member is made up solely of MF5. This is interpreted as dominant influx of organic debris from shallower parts of the glass ramp, forming lobe deposits (Veenma et al., 2022). Between the stratigraphic height of 169.73 m and 202.22 m, the upper member is dominated by MF1, occurring in all three subdivisions, with one occurrence of MF4 at height 187.73 m. The dominant occurrence of laminated fine mudstone, sometimes with basal silt lamina, is interpreted as hemipelagic sedimentation that is being reworked by bottom currents with periods of quieter conditions. During quieter periods bioturbation takes place and at 187.73 m, a calcisphere packstone is formed. Between the stratigraphic height of 226.88 m and 252.2 m, the upper member is dominated by MF6, occurring in both subdivisions, with one occurrence of MF4 at height 243.08 m and one occurrence of MF1c at height 246.33 m. The laminated sandy mudstone is interpreted as bottom current reworked sediment. The coarser microfacies may be an indication of an increase in bottom current activity.

Texture

The top left diagram shows that the texture of all samples is fine mudstone (figure 32). This is the result of the > 78 % matrix in the samples. In the diagram, all matrix is recognized as mud. However, as mentioned before, matrix is a combination of mud, cement and pore space. The actual percentage mud will therefore be lower, and the resulting texture of the samples is actually coarser than fine mud. The overestimation of mud is also the cause of the dissimilarity between the texture of the samples in this study and Veenma et al. (2022, fig. 5), who worked with some of the same samples.

The large ternary diagram shows the texture of the 20-500 μm fraction of the samples, normalised to exclude fine mud. This means that the combined percentage of silt and sand will add up to 100% (figure 32). All microfacies are clustered around the same centre. MF1 and MF5 have the widest spread. MF4 Has similar minimum and maximum values for sand but has less fine silt. MF6 has at least ~20% less sand than the other microfacies (table 5). The largest variation in the texture of the samples is in the percentage of

sand. It is observed that higher percentages of sand coincide with the presence of large scale cross-stratification (figure 31).

Table 5: Summary of the range of textures for each microfacies. Values are given in area percentage [%] (normalized to exclude mud).

Microfacies	Sand	Fine silt	Coarse silt	Sand	Fine silt	Coarse silt
	Min			*Max*		
MF1	13.66	7.36	35.14	55.89	34.69	58.12
MF4	13.99	9.52	36.24	54.23	25.65	60.36
MF5	5.95	9.57	36.76	52.24	43.80	62.55
MF6	13.39	17.22	46.96	35.83	29.16	60.34

Errors in extracting grain size of samples may result in either an over or an underestimation of the grain size. Comparing our texture data with the mud fraction of Veenma et al. (2022), who extracted most grain sizes by visual examination, leads us to believe that the matrix fraction in samples of MF4, MF5 and MF6 is overestimated by ~50% on average. The matrix in MF1 matches the results of Veenma et al. closely. MF1 is a mud rich microfacies in which the grains appear as high contrast white spots against a dark brown background. This results in precise grain recognition and explains the matching results of the grain size fractions between this study and Veenma et al. (2022). Grains in MF4, MF5 and MF6 are mostly recrystallized, reducing contrast between the grains and the background, resulting in an underestimation of the coarser fractions. This was taken into account while making interpretations of features in the rock, facies, and paleocurrent reconstruction.

Statistical parameters

The mean grain size throughout the stratigraphy is 49.8 μm. The average D99 is 126 μm. The curve of the mean follows the area percentage of the silt whereas the D99 follows the area percentage curve of the sand fraction (figure 31). 4 of the highest peaks in the D99 occur between 100 m and 160 m, coinciding with negative peaks in skewness and a microfacies of spiculitic sandy mudstone. Only the highest peak of the D99, at a height of 157 m, has a positively skewed distribution. The negative peaks in the skewness in the spiculitic sandy mudstone indicate deposition that is dominated by turbidity currents as these tend to have negatively skewed grain size distributions. Turbiditic deposition is further strengthened by the

C/M plot (figure 33). The samples fall mostly in the uniform suspension zone, parallel to the C = M line, which is typical for turbidity deposits (Passega, 1964).

Paleocurrent reconstruction

The paleocurrent reconstruction for the upper member of the McCarthy Formation was carried out using two different proxies. Both proxies show a similar trend (figure 31). The fastest flow velocities occur between 100 and 160 meters, within the spiculitic sandy mudstone, as well as peaks at a height of 78, 180 and 237 meters. The highest flow velocities all coincide with negative skewness. The curve of the flow speed, calculated using the sortable silt proxy mimics the area percentage of the very fine sand fraction (R = 0.75; supplementary materials). The sortable silt proxy shows an average current speed of 44.5 m/s, a maximum current speed of 51 m/s, and a minimum of 39 m/s. The sortable silt and very fine sand proxy shows an average current speed of 11.5 m/s, a maximum current speed of 14.8 m/s, and a minimum current speed of 9 m/s. The proxies thus indicate a range of paleocurrent speed ranging from 9 – 51 cm/s. Uncertainties in the reconstructed paleocurrent speed arise from proxy modification, grain size measurement errors, hydrodynamic properties of grains, and mixed influence of turbidity currents and bottom currents (see supplementary materials).

Interpretation of sedimentary structures

Sediment waves

We interpreted the large scale low angle cross-stratification as the fore-sets of sediment waves, following the definition by Wynn et al. (2000): "A large-scale (generally tens of metres to a few kilometres wavelength and several metres high), undulating, depositional bedform, generated beneath a current flowing at, or close to, the sea-floor". The observed height of 10–17 meters is conform other examples of sediment waves from literature (e.g. Ceri James et al., 2012; Damen et al., 2018; van Dijk et al., 2021). The slope of the cross-stratification of 6–8° is gentle compared to above mentioned examples, which we argue is the result of the finer sediment of the cliff succession compared to the examples in the literature. Sediment waves may be hundreds of meters in length and may have wavelengths of 100–1000 m (Ceri James et al., 2012; van Dijk et al., 2021). The geographic distribution of the low angle cross-stratification in the upper member of the McCarthy

Formation on a kilometer scale may therefore well resemble a sediment wave field. We argue that the sediment waves in the cliff succession are too coarse to be mud waves and too fine to be sand waves. We hereby name the cross-stratification "very large fine grained sediment waves", according to the definition by Wynn et al. (2000), combined with an adjectival modifier based on size (Ashley, 1990), and grain size information, based on Wynn and Stow (2002).

Dune scale crossbedding

We interpreted the sigmoidal features as crossbedding. The interpretation of foresets was sparked by the similarity of the sigmoidal features to other examples of crossbedding and is strengthened by the dip angle of the supposed foresets, which ranges from 13.7 – 33°. This is conform the typical 15–30° angle of foresets, corresponding to the angle of repose for sand that is saturated with water (Beakawi Al-Hashemi and Baghabra Al-Amoudi, 2018). The interpretation of cross-bedding is countered by the fact that no normal grading on the scale of thin sections was observed, since this is typical for cross-bedding. We argue that since the cross-bedding occurs on a ~30 cm scale, the grading is not observable in the thin section that covers an area of ~6 cm^2. Additionally, bioturbation is observed in thin section 126, which could have destroyed evidence of normal grading (figure 23). A second observation countering the interpretation of cross-bedding is an observed mean grainsize of 43 μm, measured with image analysis. This is problematic because the dune stability field pinches out below 100 μm (Southard and Boguchwal, 1990; Van Den Berg and Van Gelder, 1993), making it impossible to form dunes with a grainsize of 43 μm. It is possible with the used method to underestimate the grain size, as this may happen in micrographs with low contrast between grains and background (see supplementary materials). Therefore, we manually re-evaluated the micrograph from the cross-bedding. Multiple diagenetic sparite crystals, together making up one grain, were falsely recognised by ImageJ as individual grains. The actual grain size of very fine to fine sand is large enough to enable formation of dune scale cross-bedding (figure 23).

As an alternative, structural explanations for the sigmoidal features were explored. Two hypotheses were proposed, namely constructional duplexes (also known as horses) and sigmoidal extension veins (personal communication with H. De Bresser and E. Willingshofer). The first hypothesis was ruled out because of two observations. Firstly, neither striae on the exposed planes of the features, nor slip layers above and below the bed are present. Secondly, the opposing directions of the features within a

bed are implausible in constructional duplexes. The second hypothesis was also ruled out because of two observations. Sigmoidal extension veins typically have a high angle to the shear direction, whereas the angle of the sigmoidal features that were observed in the field is 13.7 – 33°. At last, the features are not mineral filled, as is common in an extensional vein.

Veenma et al. (2022) attributed the opposing directions of the foresets to the curved nature of the outcrop, with a paleocurrent perpendicular to the outcrop. Our strike/dip measurements indicate that the opposing directions are not apparent, but true orientations of the planes (Table 4). It is possible for dunes to form opposing cross-bedding but not within one set. We therefore propose that a lunate shaped dune might explain opposing cross-bedding within one set, requiring a current in only one direction. Normally trough cross-bedding formed by lunate, linguoid or crescent shaped dunes has a spread in strike/dip measurements of ~60°. However, the strike/dip measurements indicate 180° opposing crossbedding (figure 18), thus requiring a tight dune radius.

Discussion

Mixed depositional system

I interpret the upper member of the McCarthy Formation as a mixed depositional system, in which bottom currents interact with turbidity currents. I argue that the relative contribution of bottom currents and turbidity currents changes throughout the stratigraphy of the upper member. I argue that the upper member of the McCarthy Formation represents a shift from a turbidite-dominated mixed system in the cliff succession to a bottom current–dominated mixed system in the slope succession, following the classification for mixed depositional systems proposed by Rodrigues et al. (2022).

Turbiditic component

The turbiditic component is interpreted from the dominant presence of the spiculitic sandy mudstone microfacies in the cliff succession (figure 31), indicative of transport of spicules from shallower parts of the glass ramp, and from the lobe architecture of the cliff succession (Veenma et al., 2022). The Passega plot (figure 33) indicates turbiditic deposition as well.

Bottom current component

The bottom current component is interpreted from laminated mudstone facies (MF1 and MF6), present in the slope succession, and bigradational bedding that is typical for waxing and waning bottom currents (Stow and Faugères, 2008). The bigradational beds of the slope succession (figure 20, figure 21) match the bigradational facies model of a bottom current (Stow and Faugères, 2008; Rebesco et al., 2014). Some bigradational beds that are bound by an erosional surface and contain cross-lamination (figure 22) are similar to the facies model of a reworked turbidite (Shanmugam, 1997; Rodrigues et al., 2022). This is in contrast with Witmer (2007), who interpreted the bigradational bedding as tempestites. Distal tempestites closely resemble turbidites (Pérez-López and Pérez-Valera, 2012) but lack reverse grading. Since I consistently found reverse grading followed by normal grading within one bed, I interpret the bigradational bedding as bottom current deposits. The thin bedded bioturbated mudstone, often present in the slope succession (figure 19), resembles the C5 division of the bottom current facies model (Stow and Faugères, 2008) and the Te division of the Bouma sequence (Shanmugam, 1997), which I interpreted as a hemipelagite. The three above mentioned bed types are indication that the slope succession is the record of a drift. Typically, reworked turbidites are found closest to a channel, bottom current facies on drift margins and hemipelagites on the external parts of the drift (Rodrigues et al., 2022). Lateral migration of the sediment drift causes the three above mentioned facies to occur stacked on top of each other. No channel deposits were found in the fieldwork area of this study. I argue that the preservation potential of the channel deposits is lower than that of the lobe deposits due to its smaller size and erosive nature. Channel deposits may exist in shallower deposits.

Sedimentary structures

I interpreted sedimentary structures, including dune-scale cross-bedding and large-scale fine-grained sediment waves. The origin of these structures may be either turbidity current-related or bottom current-related. Ideally, more paleocurrent measurements of the dune scale cross-bedding are required to obtain statistically significant paleocurrent directions, however this is impossible due to the exposure of the rock.

Sediment waves

To resolve the origin of the sediment waves, the internal structure and the orientation relative to the ramp dip are essential criteria. Wave geometry does not discriminate between turbidity currents and bottom currents as

wave geometry is similar for turbidity current–induced sediment waves and bottom current–induced sediment waves (McCave, 2017).

Supercritical-flow bedforms

The first hypothesis is that the sediment waves are supercritical-flow bedforms, formed by turbidity currents. Common bedforms formed under supercritical flows are anti-dunes and cyclic steps. Cyclic steps have an internal structure that consist of back-set laminae with a massive base that become more stratified towards the top (Cartigny et al., 2014). This does not match the internal structure that was observed in the field. Alternatively, anti-dunes are proposed. Wave crests of anti-dunes are mostly orthogonal to the turbidity current (McCave, 2017), and the migration direction is up-ramp. This does not match the interpreted ramp dip towards the southwest of Veenma et al. (2022), but is line with a ramp dip towards the northeast, as interpreted by Trop et al. (2002).

Subcritical-flow bedforms

The second hypothesis for the origin of the sediment waves is that the sediment waves are subcritical-flow bedforms, formed by bottom currents. The internal structure of consistently to the southwest dipping foresets (figure 5, figure 6) indicates an asymmetrical sediment wave with a unidirectional current as the formation mechanism (Berne, 2000). This excludes tidal bottom currents as the formation mechanism, as tidal induced sediment waves typically contain reactivation surfaces and cross-stratification in two directions (Allen, 1980). Alternatively, contour currents are inferred as the wave forming mechanism. As these currents typically follow the contour lines of the ramp, wave crests perpendicular to the strike of the ramp are expected. Based on the inferred ramp orientation towards the southwest and foreset dipping towards the southwest, wave crests are parallel to the strike of the ramp, thereby countering the interpretation of contour currents. However, the exact ramp orientation is poorly constrained as it is based on a general thickening of the McCarthy Formation towards the southwest and of shallower formations towards the northeast (Veenma et al., 2022). Additionally, wave crests of geostrophic current–induced sediment waves may propagate at an angle of up to 45° oblique to the current (McCave, 2017). A better confinement of the ramp orientation is therefore necessary. I argue that this can be achieved by measuring more indicators of slope orientation such as slumps that are present in the upper member but have not been measured due to inaccessibility.

Another criterium to distinguish between subcritical and supercritical bedforms is the depositional environment. The 10 – 17 m height and the mudstone texture of the sediment waves in the cliff succession are typical for sedimentary structures in an unconfined depositional environment (Symons et al., 2016). This matches the interpreted lobe architecture of the cliff succession (Veenma et al., 2022). To form anti-dunes, strong highly stratified currents are required (Symons et al., 2016). It is questionable if this can be achieved on unconfined lobes.

Erosional surface

The interpreted erosional surface at the boundary between the cliff succession and the slope succession at a height of ~175 m (figure 5, figure 6) may resemble the basal erosional surface that is characteristic of a mixed depositional system. Basal erosional surfaces are on average 25–30 km wide and 50–150 km long, explaining the lateral continuity of at least 2.3 km of the erosion surface in the upper member (Rodrigues et al., 2021; Miramontes et al., 2021). The basal erosional surface is often associated with the onset of the mixed systems (Creaser et al., 2017; Sansom, 2018; Rodrigues et al., 2021). The cross-bedded sets in the cliff succession are already associated with the onset of bottom currents but it is possible that the relative contribution of bottom currents intensified during the formation of the erosion surface. Alternatively, the erosional surface may be caused by negatively climbing sedimentary structures superposed on the sediment waves (Berne, 2000). A negative climb is caused by reduced sediment supply which I argue may have resulted from a decrease in turbidity current activity.

Relative contribution of turbidity currents and bottom currents

The shift in mixed depositional system could be the consequence of an increased influence of bottom deposition or a reduced influence of turbiditic deposition. Bottom current strength is known to fluctuate (Gardner et al., 2017; Thran et al., 2018; Miramontes et al., 2019), reflected by the bigradational bedding that occurs in laminations, beds and bedsets in the slope succession (figure 20, figure 21). Therefore, it is not unlikely that the slope succession reflects an increase in bottom current activity. However, the current speed reconstructions in this study fail to show an increase in bottom current strength in the slope succession (figure 31). Additionally, no medium or large scale sedimentary structures are observed in the slope succession, pointing to lower current speeds. Instead, I argue that the

relative contribution of bottom currents increased due to a decrease in turbidity current activity. The reduced influence of turbiditic deposition is shown by the absence of sponge spicules in the slope succession (figure 31). Reduced influence of turbiditic deposition may be internally controlled by a shift in depocenter of lobe deposition, causing a reduced influence of the turbiditic component and thus favouring bottom current deposition locally. It is also possible that lobe deposition retrograded onto shallower parts of the glass ramp due to the inferred continuous transgression of the basin, which is thought to have started due to thermal subsidence of the basaltic high (MacKevett, 1970; Trop et al., 2002; Witmer, 2007) and continued during the Hettangian (Veenma et al., 2022).

Bottom current origin

So far, the general term bottom current was used to describe the reworking component of the mixed depositional system of the upper member of the McCarthy Formation. Multiple types of bottom currents have been defined in literature, comprising thermohaline-induced bottom currents, wind driven bottom currents, tide-induced currents, and baroclinic currents (e.g. internal waves) (Shanmugam, 2008). Studies have shown that all four above mentioned types of bottom currents can produce similar bedforms and traction structures (Shanmugam, 2017 and references therein), making it difficult to interpret the origin of the bottom currents in the upper member of the McCarty Formation. An important criterium to distinguish between the first two and the latter two is the flow direction relative to the orientation of the shelf, as thermohaline and wind driven currents tend to flow along the slope, whereas tide-induced and baroclinic currents tend to flow up and down-slope (Stow and Smillie, 2020).

Tide-induced currents are ruled out as the origin of the bottom current deposits. Of the four types of bottom currents, tide-induced currents may produce the most distinctive deposits, including double mud layers, flaser and lenticular bedding, and bidirectional cross-bedding directed up and down-slope (Gao and Eriksson, 1991; Shanmugam, 2003; He et al., 2008). The crescent shaped dune cross-bedding with a tight radius does not show bidirectionality. Additionally, double mud layers, flaser and lenticular bedding are absent from the stratigraphy. Shanmugam (2003) stated that tide-induced bottom currents mainly occur within submarine canyons, which are capable of focussing the tidal energy and thereby amplifying the current. If the cliff succession is indeed a the record of lobe deposition as is suggested (Veenma et al., 2022), I argue that there is not enough

confinement to focus tidal energy. Deposits of baroclinic currents, also called internalites (Pomar et al., 2012), are thought to include architectural elements that can be related to breaking of internal waves and associated turbulent flows. These include upslope dipping cross-laminated beds and downslope dipping cross-laminated beds (Bádenas et al., 2012). As these typical bidirectional cross-lamination are absent in studied stratigraphy, I argue that baroclinic currents are not the origin of the bottom current deposits. This leaves thermohaline-induced bottom currents and wind-driven bottom currents as possible formation mechanisms of the bottom current deposits in the upper member of the McCarthy Formation. Shanmugam (2021) stated however that distinguishing between thermohaline and wind driven current deposits in the rock record is impossible without establishing the paleo-water circulation pattern independently. I argue that a better understanding of the palaeogeographical setting of the McCarthy Formation on a basin scale is necessary to estimate the relative forcing of thermohaline circulation and wind.

Panthalassan circulation

The evidence of bottom currents in the upper member of the McCarthy Formation favours ocean circulation models of the Panthalassa Ocean that suggest a more vigorous bottom current activity during the Early Jurassic. The circulation patterns in the Panthalassa Ocean were first thought to have consisted of a cyclonic gyre on the northern hemisphere and an anti-cyclonic gyre on the southern hemisphere (Kutzbach et al., 1990; Chandler et al., 1992; Winguth et al., 2002; Smith et al., 2004). These studies agree qualitatively on the circulation pattern, but some studies suggest a sluggish, almost stagnant circulation with bottom current speeds ranging from 0.2 – 2 cm/s (Kutzbach et al., 1990; Winguth et al., 2002), while others suggest more vigorous rates (Smith et al., 2004). The extracted bottom current velocities from micrographs range between 9 – 51 cm/s, which is conform modern day bottom currents that may have velocities ranging from 5 – 50 cm/s, with lower velocities occurring on drifts and higher values in channels (Miramontes et al., 2019), and despite uncertainties in the used method is an order of magnitude higher than the modelled sluggish ocean circulation.

Conclusion

The upper member of the McCarthy Formation is a glass ramp, deposited in the tropical Panthalassa Ocean. I interpret the upper member of the McCarthy Formation as a mixed depositional system, where bottom currents interact with turbidity currents. The relative contribution of bottom currents and turbidity currents is thought to be variable trough time. I argue that the studied section reflects a shift from a turbidite dominated mixed system in the cliff succession to a bottom current dominated mixed system in the slope succession. This conclusion is based on the following interpretations:

1. The cliff succession is dominantly composed of spiculitic sandy mudstone (MF5). This is indicative of transport by turbidity currents since the spicule fragments originate from shallower parts of the ramp.
2. The slope succession is dominantly composed of mudstones (MF1a, b and 6a, b), that show evidence of flow by currents, such as lamination, cross-lamination, and basal silt laminae that are produced by winnowing by bottom currents. Whenever currents ceased, bioturbated mudstones (MF1c) are present.
3. In the cliff succession, I interpreted sediment waves. These are either subcritical-flow bedforms, caused by bottom currents or supercritical-flow anti-dunes, caused by turbidity currents. Discrimination between the two is difficult, as both processes produce sediment waves with similar geometries. Instead, context is necessary. It is questionable if the required current strength and stratification to form anti-dunes are achieved in the interpreted unconfined depositional environment of a lobe complex.
4. The slope succession is interpreted as the record of a sediment drift, with reworked turbidites occurring closest to the channel, bottom current facies occurring on the drift margins, and hemipelagites on the external parts of the drift. The vertical stacking of the above-mentioned facies indicates lateral migration of the sediment drift.
5. At the boundary between the cliff succession and the slope succession, an erosional surface truncates the top of the sediment waves. This laterally widespread erosional surface resembles the shift from a turbidity current dominated to a bottom current dominated system. The cause of the erosion is either the onset of bottom currents, or reduced sedimentation rates as the result of reduced turbidity current activity.

We interpret a combination of an onset in bottom current activity and a decrease in turbiditic deposition, in turn related to either retrogradation of the ramp or avulsion of the lobe complex, to explain the transition between the cliff succession and the slope succession.

The origin of the bottom currents is thought to be thermohaline or wind driven. Characteristic facies for tidalites or internalites are absent from the stratigraphy. Further distinction between thermohaline and wind-driven currents can be made with improved knowledge of the paleogeographic setting of the McCarthy Formation, arguably of Wrangellia.

The evidence of bottom currents in the upper member of the McCarthy Formation favours ocean circulation models of the Panthalassa Ocean that suggest a more vigorous bottom current activity during the Early Jurassic. Bottom currents were quantified using proxies to reconstruct paleocurrent speed, which resulted in velocities ranging from 9 – 51 cm/s. Despite uncertainties in the used method, these values are conform modern day bottom current speeds. This information may be used to improve palaeoceanographic models of the Panthalassa Ocean.

References

Aberhan, M., 1998, Paleobiogeographic Patterns of Pectinoid Bivalves and the Early Jurassic Tectonic Evolution of Western Canadian Terranes: PALAIOS, v. 13, p. 129–148, doi:10.2307/3515485.

Ahr, W.M., 1973, Carbonate Ramp--Alternative to Shelf Model: ABSTRACT: AAPG Bulletin, v. 57, p. 1826–1826.

Allen, J.R.L., 1980, Sand waves: A model of origin and internal structure: Sedimentary Geology, v. 26, p. 281–328, doi:10.1016/0037-0738(80)90022-6.

Alonso, B. et al., 2021, Paleoceanographic and paleoclimatic variability in the Western Mediterranean during the last 25 cal. kyr BP. New insights from contourite drifts: Marine Geology, v. 437, p. 106488, doi:10.1016/j.margeo.2021.106488.

Arias, C., 2008, Palaeoceanography and biogeography in the Early Jurassic Panthalassa and Tethys Oceans: Gondwana Research, v. 14, p. 306–315, doi:10.1016/j.gr.2008.03.004.

Armstrong, A., K., MacKevett, E.M., and Silberling, N.J., 1969, THE CHITISTONE AND NIZINA LIMESTONES OF PART OF THE SOUTHERN WRANGELL MOUNTAINS, ALASKA - A PRELIMINARY REPORT STRESSING CARBONATE PETROGRAPHY AND DEPOSITIONAL ENVIRONMENTS:

Ashley, G.M., 1990, Classification of large-scale subaqueous bedforms; a new look at an old problem: Journal of Sedimentary Research, v. 60, p. 160–172, doi:10.2110/jsr.60.160.

Bádenas, B., Pomar, L., Aurell, M., and Morsilli, M., 2012, A facies model for internalites (internal wave deposits) on a gently sloping carbonate ramp (Upper Jurassic, Ricla, NE Spain): Sedimentary Geology, v. 271–272, p. 44–57, doi:10.1016/j.sedgeo.2012.05.020.

Bahr, A. et al., 2014, Deciphering bottom current velocity and paleoclimate signals from contourite deposits in the Gulf of Cádiz during the last 140 kyr: An inorganic geochemical approach: Geochemistry, Geophysics, Geosystems, v. 15, p. 3145–3160, doi:10.1002/2014GC005356.

Barnolas, A., and Llave, E., 2012, Contourites, turbidites and mass wasting deposits in the Middle and Upper Jurassic of the Majorca Island (Spain): v. 13, p. 4.

Beakawi Al-Hashemi, H.M., and Baghabra Al-Amoudi, O.S., 2018, A review on the angle of repose of granular materials: Powder Technology, v. 330, p. 397–417, doi:10.1016/j.powtec.2018.02.003.

Berne, S., 2000, Architecture, dynamics and preservation of marine sand waves (large dunes):

Blott, S.J., and Pye, K., 2001, GRADISTAT: a grain size distribution and statistics package for the analysis of unconsolidated sediments: Earth Surface Processes and Landforms, v. 26, p. 1237–1248, doi:10.1002/esp.261.

Burchette, T.P., and Wright, V.P., 1992, Carbonate ramp depositional systems: Sedimentary Geology, v. 79, p. 3–57, doi:10.1016/0037-0738(92)90003-A.

Butler, R.F., Gehrels, G.E., and Bazard, D.R., 1997, Paleomagnetism of Paleozoic strata of the Alexander terrane, southeastern Alaska: GSA Bulletin, v. 109, p. 1372–1388, doi:10.1130/0016-7606(1997)109<1372:POPSOT>2.3.CO;2.

Campbell, C.V., 1967, Lamina, Laminaset, Bed and Bedset: Sedimentology, v. 8, p. 7–26, doi:10.1111/j.1365-3091.1967.tb01301.x.

Cartigny, M.J.B., Ventra, D., Postma, G., and van Den Berg, J.H., 2014, Morphodynamics and sedimentary structures of bedforms under supercritical-flow conditions: New insights from flume experiments: Sedimentology, v. 61, p. 712–748, doi:10.1111/sed.12076.

Caruthers, A.H. et al., 2022, New evidence for a long Rhaetian from a Panthalassan succession (Wrangell Mountains, Alaska) and regional differences in carbon cycle perturbations at the Triassic-Jurassic transition: Earth and Planetary Science Letters, v. 577, p. 117262, doi:10.1016/j.epsl.2021.117262.

Caruthers, A.H., and Stanley, G.D., 2008, Late Triassic silicified shallow-water corals and other marine fossils from Wrangellia and the Alexander terrane, Alaska, and Vancouver Island, British Columbia:, doi:10.1130/2008.442(10).

Cauxeiro, C., Lopez, M., Hernández-Molina, J., Miguel, A., Cauxeiro, G., and Caetano, V., 2020, Contourite vs Turbidite Outcrop and Seismic Architectures: Angolan Mineral, Oil & Gas Journal, v. 1, p. 20–26, doi:10.47444/amogj.v1i1.9.

Ceri James, J.W., Mackie, A.S.Y., Rees, E.I.S., and Darbyshire, T., 2012, 12 - Sand Wave Field: The OBel Sands, Bristol Channel, UK, in Harris, P.T. and Baker, E.K. eds., Seafloor Geomorphology as Benthic

Habitat, London, Elsevier, p. 227–239, doi:10.1016/B978-0-12-385140-6.00012-8.

Chandler, M.A., RIND, D., and RUEDY, R., 1992, Pangaean climate during the Early Jurassic: GCM simulations and the sedimentary record of paleoclimate: GSA Bulletin, v. 104, p. 543–559, doi:10.1130/0016-7606(1992)104<0543:PCDTEJ>2.3.CO;2.

Creaser, A., Hernández-Molina, F.J., Badalini, G., Thompson, P., Walker, R., Soto, M., and Conti, B., 2017, A Late Cretaceous mixed (turbidite-contourite) system along the Uruguayan Margin: Sedimentary and palaeoceanographic implications: Marine Geology, v. 390, p. 234–253, doi:10.1016/j.margeo.2017.07.004.

Csejtey Jr., B., Cox, D.P., Evarts, R.C., Stricker, G.D., and Foster, H.L., 1982, The Cenozoic Denali Fault System and the Cretaceous accretionary development of southern Alaska: Journal of Geophysical Research: Solid Earth, v. 87, p. 3741–3754, doi:10.1029/JB087iB05p03741.

Damen, J.M., van Dijk, T. a. G.P., and Hulscher, S.J.M.H., 2018, Spatially Varying Environmental Properties Controlling Observed Sand Wave Morphology: Journal of Geophysical Research: Earth Surface, v. 123, p. 262–280, doi:10.1002/2017JF004322.

Dera, G., and Donnadieu, Y., 2012, Modeling evidences for global warming, Arctic seawater freshening, and sluggish oceanic circulation during the Early Toarcian anoxic event: Paleoceanography, v. 27, doi:10.1029/2012PA002283.

van Dijk, T.A.G.P., Best, J., and Baas, A.C.W., 2021, Subaqueous and Subaerial Depositional Bedforms, in Alderton, D. and Elias, S.A. eds., Encyclopedia of Geology (Second Edition), Oxford, Academic Press, p. 771–786, doi:10.1016/B978-0-08-102908-4.00187-9.

Folk, R.L., and Ward, W.C., 1957, Brazos River bar [Texas]; a study in the significance of grain size parameters: Journal of Sedimentary Research, v. 27, p. 3–26, doi:10.1306/74D70646-2B21-11D7-8648000102C1865D.

Frébourg, G., Ruppel, S.C., and Rowe, H., 2013, Chapter 4: Sedimentology of the Haynesville (Upper Kimmeridgian) and Bossier (Tithonian) Formations, in the Western Haynesville Basin, Texas, U.S.A.: , p. 47–67.

Gao, Z.-Z., and Eriksson, K.A., 1991, Internal-tide deposits in an Ordovician submarine channel: Previously unrecognized facies? Geology, v. 19, p. 734–737, doi:10.1130/0091-7613(1991)019<0734:ITDIAO>2.3.CO;2.

Gardner, W.D., Tucholke, B.E., Richardson, M.J., and Biscaye, P.E., 2017, Benthic storms, nepheloid layers, and linkage with upper ocean dynamics in the western North Atlantic: Marine Geology, v. 385, p. 304–327, doi:10.1016/j.margeo.2016.12.012.

Gates, L.M., James, N.P., and Beauchamp, B., 2004, A glass ramp: shallow-water Permian spiculitic chert sedimentation, Sverdrup Basin, Arctic Canada: Sedimentary Geology, v. 168, p. 125–147, doi:10.1016/j.sedgeo.2004.03.008.

Georgiev, G., and Botoucharov, N., 2007, Are there Middle Jurassic contourites in the Tarnovo depression (Southern Moesian platform margin)? Geological Society, London, Special Publications, v. 276, p. 283–298, doi:10.1144/GSL.SP.2007.276.01.14.

Greene, A.R., Scoates, J.S., Weis, D., Katvala, E.C., Israel, S., and Nixon, G.T., 2010, The architecture of oceanic plateaus revealed by the volcanic stratigraphy of the accreted Wrangellia oceanic plateau: Geosphere, v. 6, p. 47–73, doi:10.1130/GES00212.1.

He, Y., Gao, Z., Luo, J., Luo, S., and Liu, X., 2008, Characteristics of internal-wave and internal-tide deposits and their hydrocarbon potential: Petroleum Science, v. 5, p. 37–44, doi:10.1007/s12182-008-0006-4.

Heinhuis, Y., 2020, Architecture of a glass ramp: The McCarthy Formation, Southcentral Alaska. [Bachelor's dissertation]: Utrecht University, 38 p.

Hillhouse, J.W., and Coe, R.S., 1994, Paleomagnetic data from Alaska: Geology of North America, https://websites.pmc.ucsc.edu/~rcoe/coepubs/coe49.pdf (accessed April 2020).

Hüneke, H., and Stow, D.A.V., 2008, Chapter 17 Identification of Ancient Contourites: Problems and Palaeoceanographic Significance, *in* Developments in Sedimentology, Elsevier, v. 60, p. 323–344, doi:10.1016/S0070-4571(08)10017-6.

Isozaki, Y., 1997, Permo-Triassic Boundary Superanoxia and Stratified Superocean: Records from Lost Deep Sea: Science, v. 276, p. 235–238, doi:10.1126/science.276.5310.235.

Jones, D.L., Silberling, N.J., and Hillhouse, J., 1977, Wrangellia—A displaced terrane in northwestern North America: Canadian Journal of Earth Sciences, v. 14, p. 2565–2577, doi:10.1139/e77-222.

Kiehl, J.T., and Shields, C.A., 2005, Climate simulation of the latest Permian: Implications for mass extinction: Geology, v. 33, p. 757–760, doi:10.1130/G21654.1.

Kutzbach, J.E., Guetter, P.J., and Washington, W.M., 1990, Simulated circulation of an idealized ocean for Pangaean time: Paleoceanography, v. 5, p. 299–317, doi:10.1029/PA005i003p00299.

MacKevett, E.M., 1970, Geology of the McCarthy B-4 Quadrangle, Alaska: U.S. Government Printing Office, 320 p.

MacKevett, E.M., 1963, Preliminary geologic map of the McCarthy C-5 quadrangle, Alaska: IMAP, doi:10.3133/i406.

MARTIN, G.C., 1916, Triassic rocks of Alaska1: GSA Bulletin, v. 27, p. 685–718, doi:10.1130/GSAB-27-685.

McCave, I.N., 2017, Formation of sediment waves by turbidity currents and geostrophic flows: A discussion: Marine Geology, v. 390, p. 89–93, doi:10.1016/j.margeo.2017.05.003.

McCave, I.N., Thornalley, D.J.R., and Hall, I.R., 2017, Relation of sortable silt grain-size to deep-sea current speeds: Calibration of the 'Mud Current Meter': Deep Sea Research Part I: Oceanographic Research Papers, v. 127, p. 1–12, doi:10.1016/j.dsr.2017.07.003.

McClelland, W.C., Gehrels, G.E., and Saleeby, J.B., 1992, Upper Jurassic-Lower Cretaceous basinal strata along the Cordilleran Margin: Implications for the accretionary history of the Alexander-Wrangellia-Peninsular Terrane: Tectonics, v. 11, p. 823–835, doi:10.1029/92TC00241.

Miramontes, E. et al., 2021, Contourite and mixed turbidite-contourite systems in the Mozambique Channel (SW Indian Ocean): Link between geometry, sediment characteristics and modelled bottom currents: Marine Geology, v. 437, p. 106502, doi:10.1016/j.margeo.2021.106502.

Miramontes, E., Garreau, P., Caillaud, M., Jouet, G., Pellen, R., Hernández-Molina, F.J., Clare, M.A., and Cattaneo, A., 2019, Contourite distribution and bottom currents in the NW Mediterranean Sea: Coupling seafloor geomorphology and hydrodynamic modelling: Geomorphology, v. 333, p. 43–60, doi:10.1016/j.geomorph.2019.02.030.

Nokleberg, W.J., Plafker, G., and Wilson, F.H., 1994, Geology of south-central Alaska, in Plafker, G. and Berg, H.C. eds., The Geology of Alaska, Geological Society of America, v. G-1, p. 0, doi:10.1130/DNAG-GNA-G1.311.

Passega, R., 1964, Grain size representation by CM patterns as a geologic tool: Journal of Sedimentary Research, v. 34, p. 830–847, doi:10.1306/74D711A4-2B21-11D7-8648000102C1865D.

Paz, M., Buatois, L.A., Mángano, M.G., Desjardins, P.R., Notta, R., González Tomassini, F., Carmona, N.B., and Minisini, D., 2022, Organic-rich, fine-grained contourites in an epicontinental basin: The Upper Jurassic-Lower Cretaceous Vaca Muerta Formation, Argentina: Marine and Petroleum Geology, v. 142, p. 105757, doi:10.1016/j.marpetgeo.2022.105757.

Pérez-López, A., and Pérez-Valera, F., 2012, Tempestite facies models for the epicontinental Triassic carbonates of the Betic Cordillera (southern Spain): Sedimentology, v. 59, p. 646–678, doi:10.1111/j.1365-3091.2011.01270.x.

Pomar, L., Morsilli, M., Hallock, P., and Bádenas, B., 2012, Internal waves, an under-explored source of turbulence events in the sedimentary record: Earth-Science Reviews, v. 111, p. 56–81, doi:10.1016/j.earscirev.2011.12.005.

Rahmstorf, S., 2002, Ocean circulation and climate during the past 120,000 years: Nature, v. 419, p. 207–214, doi:10.1038/nature01090.

Read, J.F., 1985, Carbonate Platform Facies Models: AAPG Bulletin, v. 69, p. 1–21, doi:10.1306/AD461B79-16F7-11D7-8645000102C1865D.

Read, J.F., 1982, Carbonate platforms of passive (extensional) continental margins: Types, characteristics and evolution - ScienceDirect:, https://www-sciencedirect-com.proxy.library.uu.nl/science/article/pii/0040195182901299 (accessed July 2020).

Rebesco, M., Hernández-Molina, F.J., Van Rooij, D., and Wåhlin, A., 2014, Contourites and associated sediments controlled by deep-water circulation processes: State-of-the-art and future considerations: Marine Geology, v. 352, p. 111–154, doi:10.1016/j.margeo.2014.03.011.

Ritterbush, K., 2019, Sponge meadows and glass ramps: State shifts and regime change: Palaeogeography, Palaeoclimatology, Palaeoecology, v. 513, p. 116–131, doi:10.1016/j.palaeo.2018.08.009.

Rodrigues, S., Hernández-Molina, F.J., Fonnesu, M., Miramontes, E., Rebesco, M., and Campbell, D.C., 2022, A new classification system for mixed (turbidite-contourite) depositional systems: Examples, conceptual models and diagnostic criteria for modern and ancient records: Earth-Science Reviews, v. 230, p. 104030, doi:10.1016/j.earscirev.2022.104030.

Rodrigues, S., Hernández-Molina, F.J., and Kirby, A., 2021, A Late Cretaceous mixed (turbidite-contourite) system along the Argentine Margin: Paleoceanographic and conceptual implications: Marine and Petroleum Geology, v. 123, p. 104768, doi:10.1016/j.marpetgeo.2020.104768.

Ruvalcaba Baroni, I., Pohl, A., van Helmond, N.A.G.M., Papadomanolaki, N.M., Coe, A.L., Cohen, A.S., van de Schootbrugge, B., Donnadieu, Y., and Slomp, C.P., 2018, Ocean Circulation in the Toarcian (Early Jurassic): A Key Control on Deoxygenation and Carbon Burial on the European Shelf: Paleoceanography and Paleoclimatology, v. 33, p. 994–1012, doi:10.1029/2018PA003394.

Sansom, P., 2018, Hybrid turbidite–contourite systems of the Tanzanian margin: Petroleum Geoscience, v. 24, p. 258–276, doi:10.1144/petgeo2018-044.

Saunders, A., and Reichow, M., 2009, The Siberian Traps and the End-Permian mass extinction: a critical review: Chinese Science Bulletin, v. 54, p. 20–37, doi:10.1007/s11434-008-0543-7.

Shanmugam, G., 2008, Chapter 5 Deep-water Bottom Currents and their Deposits, in Developments in Sedimentology, Elsevier, v. 60, p. 59–81, doi:10.1016/S0070-4571(08)10005-X.

Shanmugam, G., 2017, Chapter 9 - The Contourite Problem, in Mazumder, R. ed., Sediment Provenance, Elsevier, p. 183–254, doi:10.1016/B978-0-12-803386-9.00009-5.

Shanmugam, G., 2003, Deep-marine tidal bottom currents and their reworked sands in modern and ancient submarine canyons: Marine and Petroleum Geology, v. 20, p. 471–491, doi:10.1016/S0264-8172(03)00063-1.

Shanmugam, G., 1997, The Bouma Sequence and the turbidite mind set: Earth-Science Reviews, v. 42, p. 201–229, doi:10.1016/S0012-8252(97)81858-2.

Shanmugam, G., 2021, The turbidite-contourite-tidalite-baroclinite-hybridite problem: orthodoxy vs. empirical evidence behind the "Bouma Sequence": Journal of Palaeogeography, v. 10, p. 9, doi:10.1186/s42501-021-00085-1.

Silberling, N.J., Grant-Mackie, J.A., and Nichols, K.M., 1997, The Late Triassic bivalve Monotis in accreted terranes of Alaska:, doi:10.3133/b2151.

Smillie, Z., and Stow, D., 2017, Contourites of the Gulf of Cadiz: geochemical and paleoclimate proxies: Daphne Jackson Research Conference.

Smith, R.S., Dubois, C., and Marotzke, J., 2004, Ocean circulation and climate in an idealised Pangean OAGCM: Geophysical Research Letters, v. 31, doi:10.1029/2004GL020643.

Southard, J.B., and Boguchwal, L.A., 1990, Bed configuration in steady unidirectional water flows; Part 2, Synthesis of flume data: Journal of Sedimentary Research, v. 60, p. 658–679, doi:10.1306/212F9241-2B24-11D7-8648000102C1865D.

Stow, D.A.V., and Faugères, J.-C., 2008, Chapter 13 Contourite Facies and the Facies Model, *in* Rebesco, M. and Camerlenghi, A. eds., Developments in Sedimentology, Elsevier, Contourites, v. 60, p. 223–256, doi:10.1016/S0070-4571(08)10013-9.

Stow, D., and Smillie, Z., 2020, Distinguishing between Deep-Water Sediment Facies: Turbidites, Contourites and Hemipelagites: Geosciences, v. 10, p. 68, doi:10.3390/geosciences10020068.

Symons, W.O., Sumner, E.J., Talling, P.J., Cartigny, M.J.B., and Clare, M.A., 2016, Large-scale sediment waves and scours on the modern seafloor and their implications for the prevalence of supercritical flows: Marine Geology, v. 371, p. 130–148, doi:10.1016/j.margeo.2015.11.009.

Thiéblemont, A., Hernández-Molina, F.J., Ponte, J.-P., Robin, C., Guillocheau, F., Cazzola, C., and Raisson, F., 2020, Seismic stratigraphic framework and depositional history for Cretaceous and Cenozoic contourite depositional systems of the Mozambique Channel, SW Indian Ocean: Marine Geology, v. 425, p. 106192, doi:10.1016/j.margeo.2020.106192.

Thran, A.C., Dutkiewicz, A., Spence, P., and Müller, R.D., 2018, Controls on the global distribution of contourite drifts: Insights from an eddy-resolving ocean model: Earth and Planetary Science Letters, v. 489, p. 228–240, doi:10.1016/j.epsl.2018.02.044.

Trop, J.M., Ridgway, K.D., Manuszak, J.D., and Layer, P., 2002, Mesozoic sedimentary-basin development on the allochthonous Wrangellia composite terrane, Wrangell Mountains basin, Alaska: A long-term record of terrane migration and arc construction: GSA Bulletin, v. 114, p. 693–717, doi:10.1130/0016-7606(2002)114<0693:MSBDOT>2.0.CO;2.

Van Den Berg, J.H., and Van Gelder, A., 1993, A New Bedform Stability Diagram, with Emphasis on the Transition of Ripples to Plane Bed

in Flows over Fine Sand and Silt, *in* Alluvial Sedimentation, John Wiley & Sons, Ltd, p. 11–21, doi:10.1002/9781444303995.ch2.

Veenma, Y.P., McCabe, K., Caruthers, A.H., Aberhan, M., Golding, M., Marroquín, S.M., Owens, J.D., Them, T.R., II, Gill, B.C., and Trabucho Alexandre, J.P., 2022, The glass ramp of Wrangellia: Late Triassic to Early Jurassic outer ramp environments of the McCarthy Formation, Alaska, U.S.A.: Journal of Sedimentary Research, v. 92, p. 896–919, doi:10.2110/jsr.2022.004.

Viana, A.R., and Rebesco, M. (Eds.), 2007, Economic and Palaeoceanographic Significance of Contourite Deposits: Geological Society of London, 368 p.

Wentworth, C.K., 1933, Fundamental Limits to the Sizes of Clastic Grains: Science, v. 77, p. 633–634.

Winguth, A.M.E., Heinze, C., Kutzbach, J.E., Maier-Reimer, E., Mikolajewicz, U., Rowley, D., Rees, A., and Ziegler, A.M., 2002, Simulated warm polar currents during the middle Permian: Paleoceanography, v. 17, p. 9-1-9–18, doi:10.1029/2001PA000646.

Witmer, J.W., 2007, SEDIMENTOLOGY AND STRATIGRAPHY OF THE UPPER TRIASSIC–LOWER JURASSIC McCARTHY FORMATION, WRANGELL–ST. ELIAS MOUNTAINS, SOUTH–CENTRAL ALASKA: Bucknell University.

Wright, V.P., and Burchette, T.P., 1998, Carbonate ramps: an introduction: Geological Society, London, Special Publications, v. 149, p. 1–5, doi:10.1144/GSL.SP.1999.149.01.01.

Wu, S. et al., 2021, Orbital- and millennial-scale Antarctic Circumpolar Current variability in Drake Passage over the past 140,000 years: Nature Communications, v. 12, p. 3948, doi:10.1038/s41467-021-24264-9.

Wynn, R.B., and Stow, D.A.V., 2002, Classification and characterisation of deep-water sediment waves: Marine Geology, v. 192, p. 7–22, doi:10.1016/S0025-3227(02)00547-9.

Wynn, R.B., Weaver, P.P.E., Ercilla, G., Stow, D.A.V., and Masson, D.G., 2000, Sedimentary processes in the Selvage sediment-wave field, NE Atlantic: new insights into the formation of sediment waves by turbidity currents: Sedimentology, v. 47, p. 1181–1197, doi:10.1046/j.1365-3091.2000.00348.x.
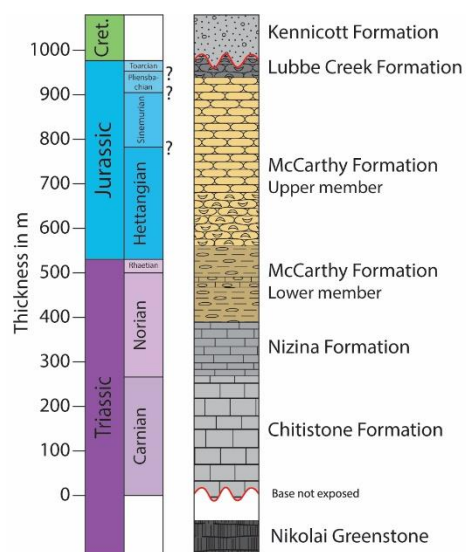
Figure 1: Stratigraphic framework of the Triassic–Jurassic of the Wrangell Mountains, based on MacKevett (1970), Trop et al. (2002), Witmer (2007), and Caruthers et al. (2022), modified from Veenma et al. (2022).
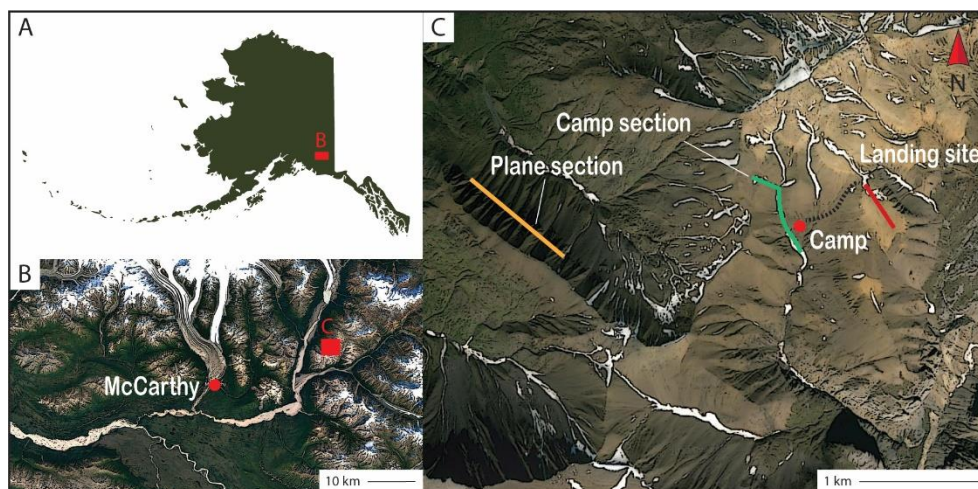
Figure 2: The upper member of the McCarthy Formation is exposed on the slopes of the Chitistone Mountain in the Wrangell mountains (B), Southcentral Alaska (A), ~25 km east-northeast of McCarthy. The upper member is studied along an unnamed tributary of the Grotto Creek and from a Piper cub airplane (C).
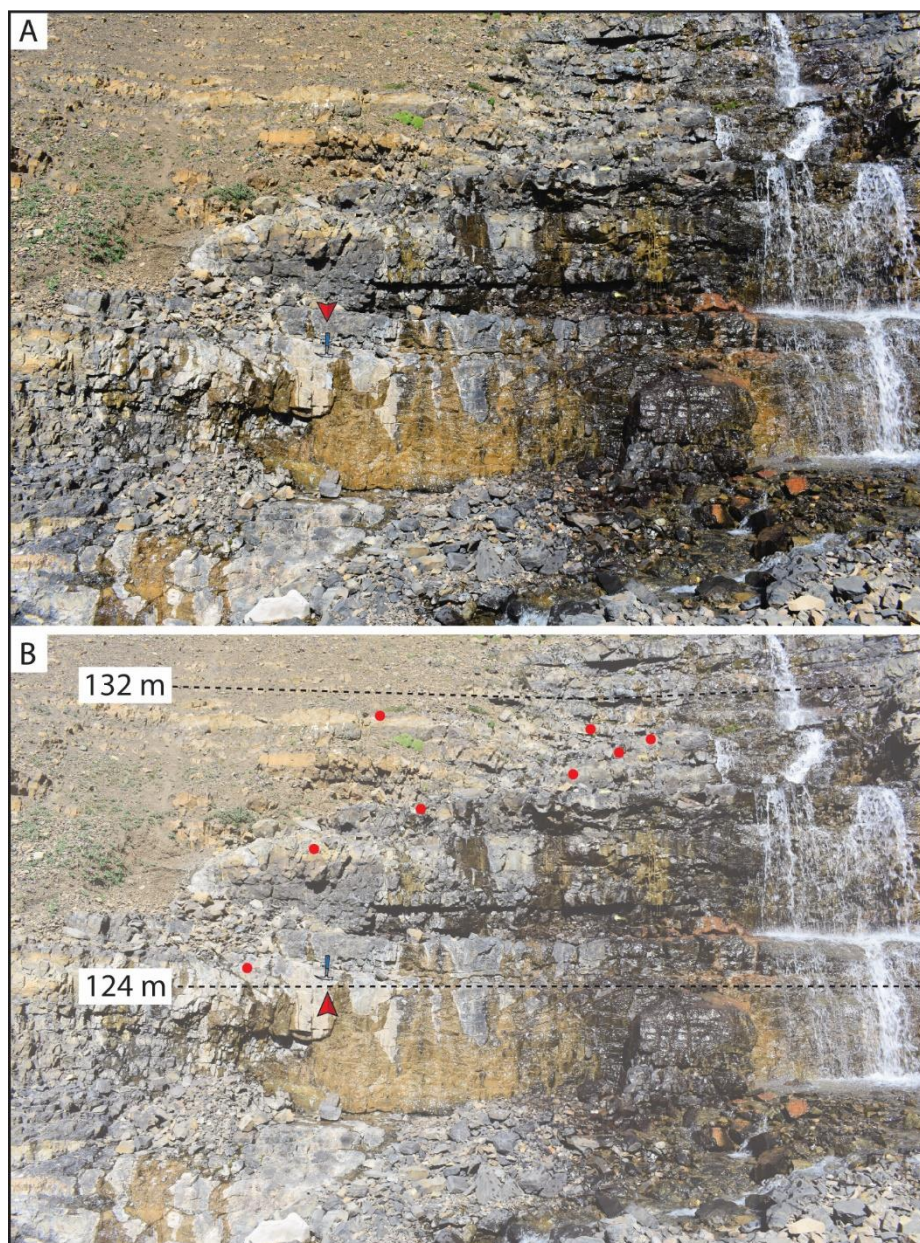
Figure 3: Between stratigraphic height 124 – 132 m, sigmoidal features were observed **A.** Outcrop, not annotated. **B.** Red dots mark beds with sigmoidal features. Geological hammer for scale, indicated by red arrow.
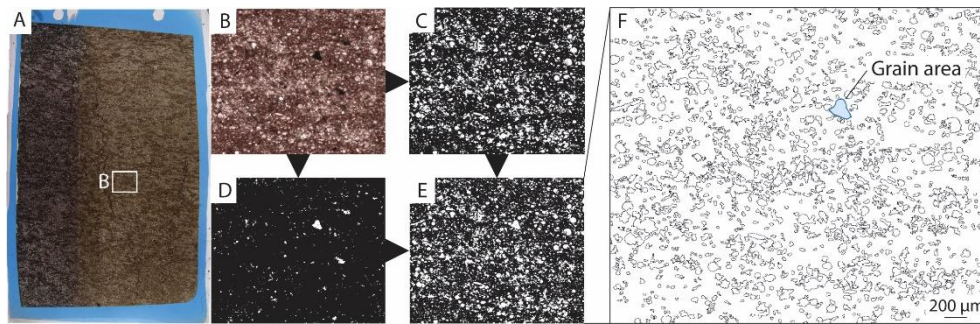
Figure 4: From a thin section (A), a 25× magnification micrograph (B) is taken using a petrographic microscope. Brightness threshold are then applied to extract light and dark grains (C, D). The images are subsequently spliced (E). Finally, the area of each grain is measured (F).
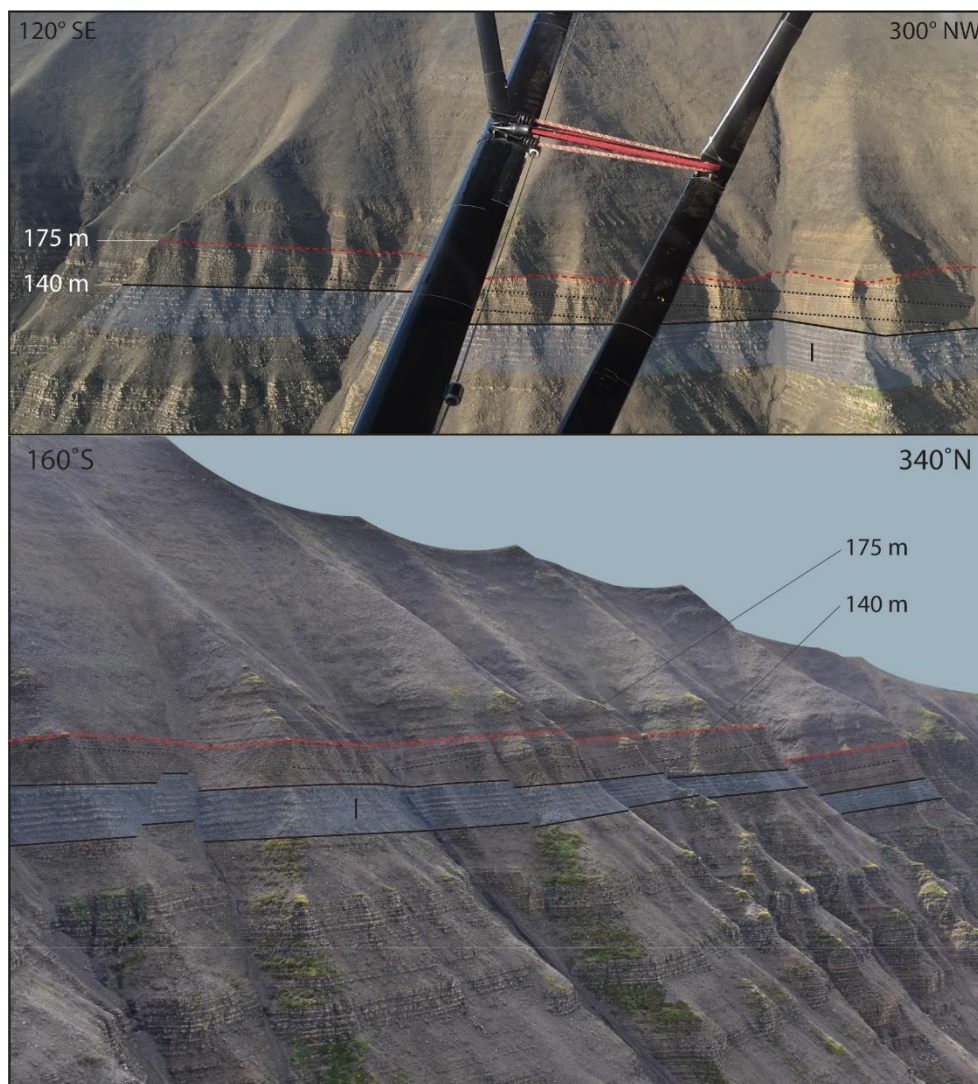
Figure 5: 2.3 km towards the southwest of the Grotto Creek, low angle cross-stratification was observed. The section was correlated to the Grotto Creek using distinct horizontal bedding pattern, indicated with Roman numeral I. Black dotted line marks cross-stratification. Red dotted line marks ~175 m, the transition from cliff forming succession to slope forming succession.
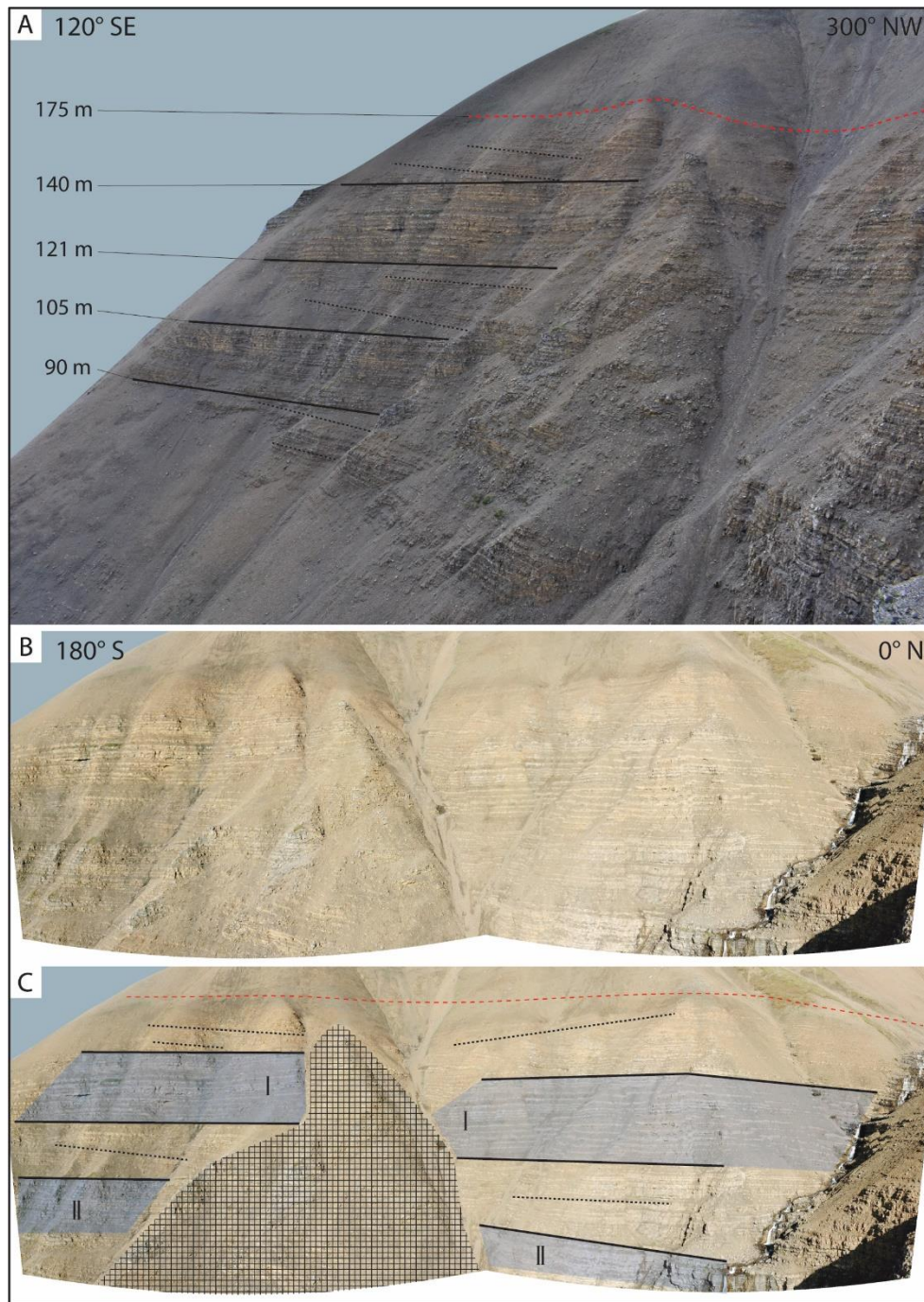
Figure 6: The upper member of the McCarthy Formation in the Grotto Creek section contains three sets of low angle cross-stratification. **A.** The three sets of cross-stratification. The red dotted line marks the height where the cliff forming succession transitions into the slope forming succession at a height of ~175 m. Black dotted lines mark cross stratification. **B.** Panorama panel of succession with low angle cross-stratification (no annotations). **C.** Cross-stratification correlated to the creek, across a collapsed part of the outcrop (hashed area). Roman numerals indicate distinct horizontal bedding patterns that facilitated the correlation. Black dotted lines mark cross-stratification. Red dotted line marks transition.

Figure 7: The upper set of the low angle cross-stratification is present in the Grotto Creek, camp section (figure 6) and 2.3 km towards the west in the plane section (figure 5).
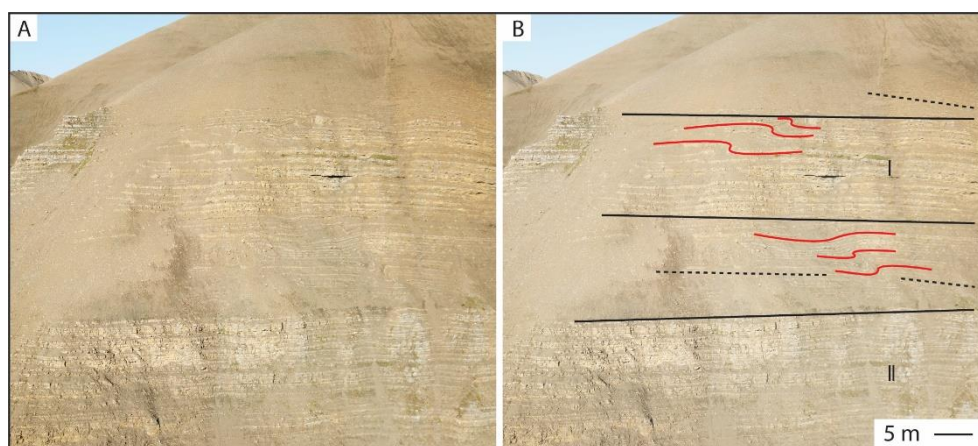
Figure 8: The cliff forming succession contains slumps in both the (sub)horizontal strata as well as the cross stratified strata.

Figure 9: The section with low angle cross-stratification (A) contains ~8 cm thick concretionary beds. The section with subhorizontal bedding (B) contains ~30 cm thick buff-coloured concretions. In between the concretions, the bedding is thinner and dark grey coloured. Concretions indicated with white dotted lines.
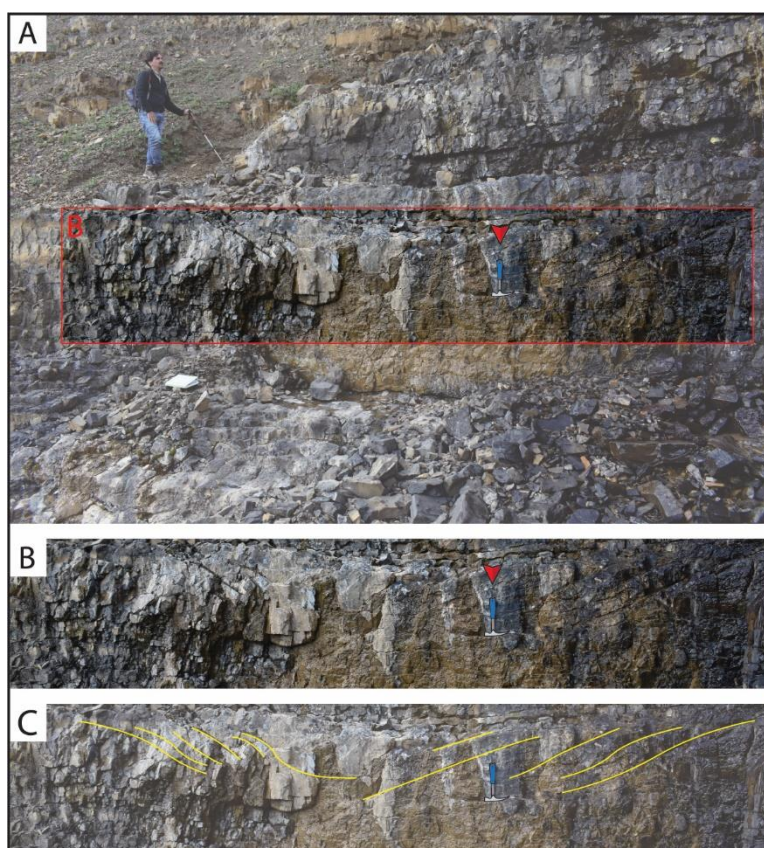
Figure 10: Sigmoidal features at 124 m. **A.** Outcrop photograph. Red box indicates area of interest. **B.** Sigmoidal features (no annotations). Geological hammer for scale, indicated with red arrow. **C.** Sigmoidal features with opposing orientations are marked by yellow lines.
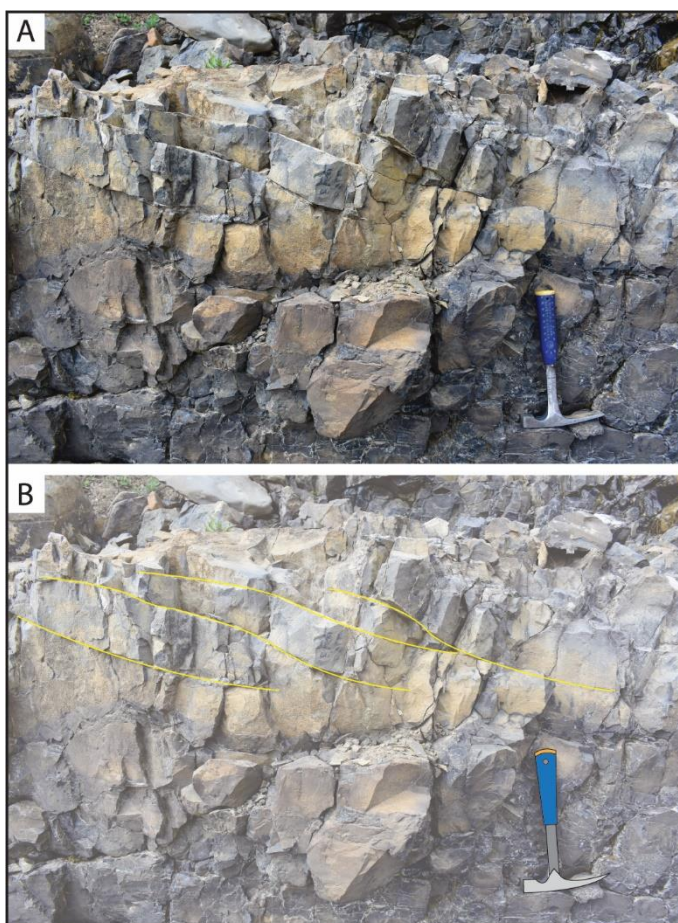
Figure 11: Sigmoidal features at 126 m. **A.** Sigmoidal features (no annotations). **B.** Sigmoidal features (yellow) downlap on bedding plane and on each other. Geological hammer for scale.

Figure 12: Sigmoidal features at 127 m. **A.** Sigmoidal features (no annotations). **B.** Sigmoidal features (yellow). Geological hammer for scale.
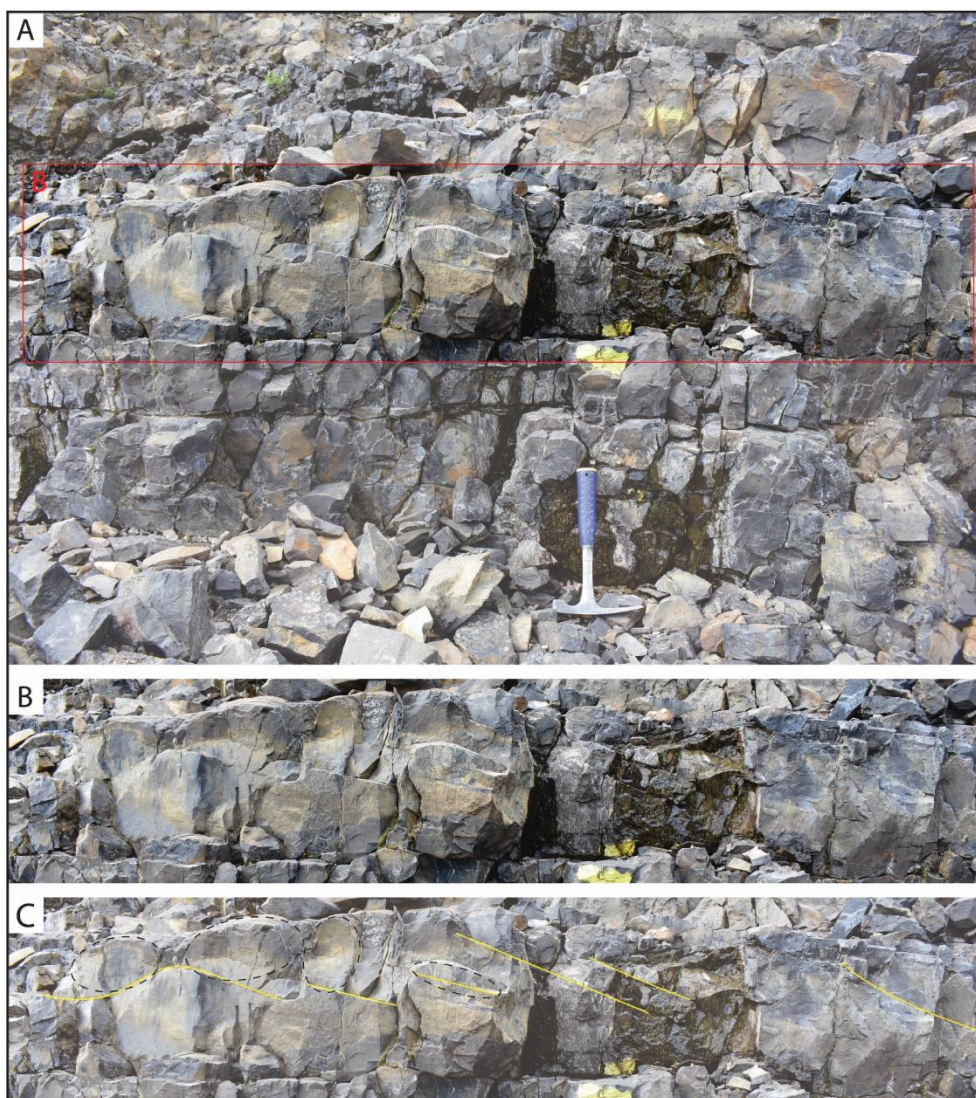
Figure 13: Sigmoidal features at 128.5 m. **A.** Outcrop. Red box indicates area of interest. Geological hammer for scale. **B.** Sigmoidal features and concretions (no annotations). **C.** Sigmoidal features are marked with yellow lines. Concretions are marked with black dotted lines.
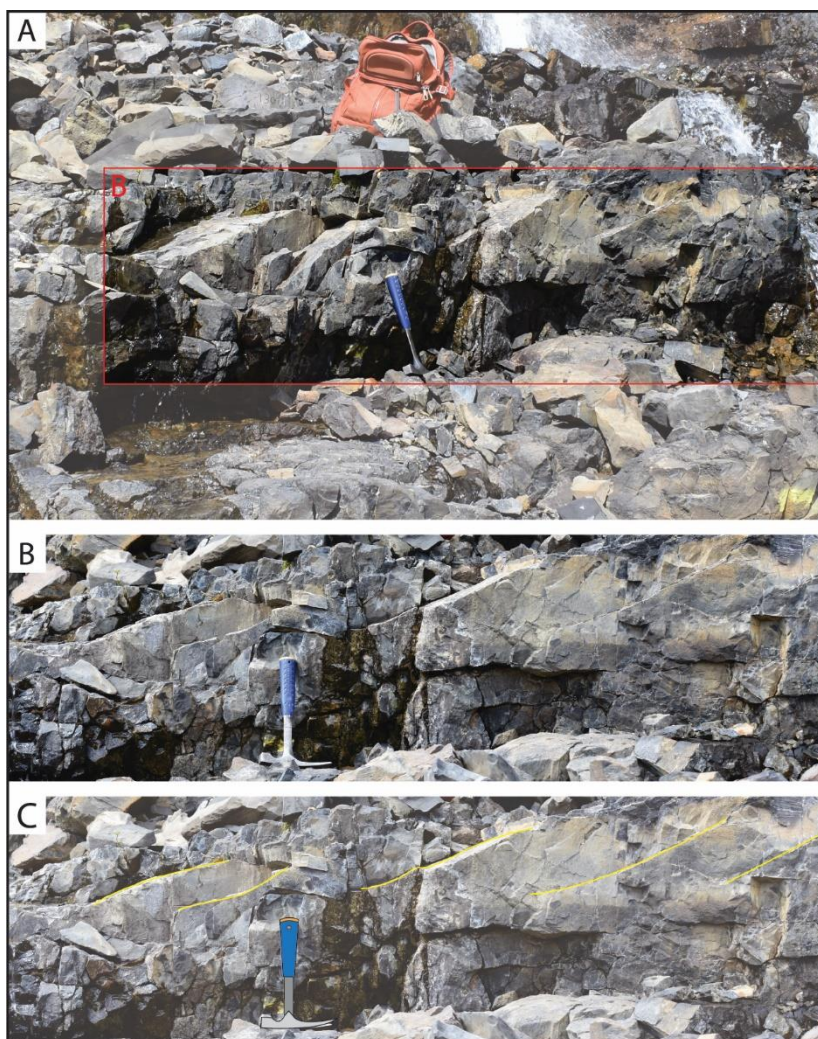
Figure 14: Sigmoidal features at 129.5 m. **A.** Outcrop. Red box indicates area of interest. **B.** Sigmoidal features (no annotations). **C.** Sigmoidal features are marked with yellow lines. Geological hammer for scale.
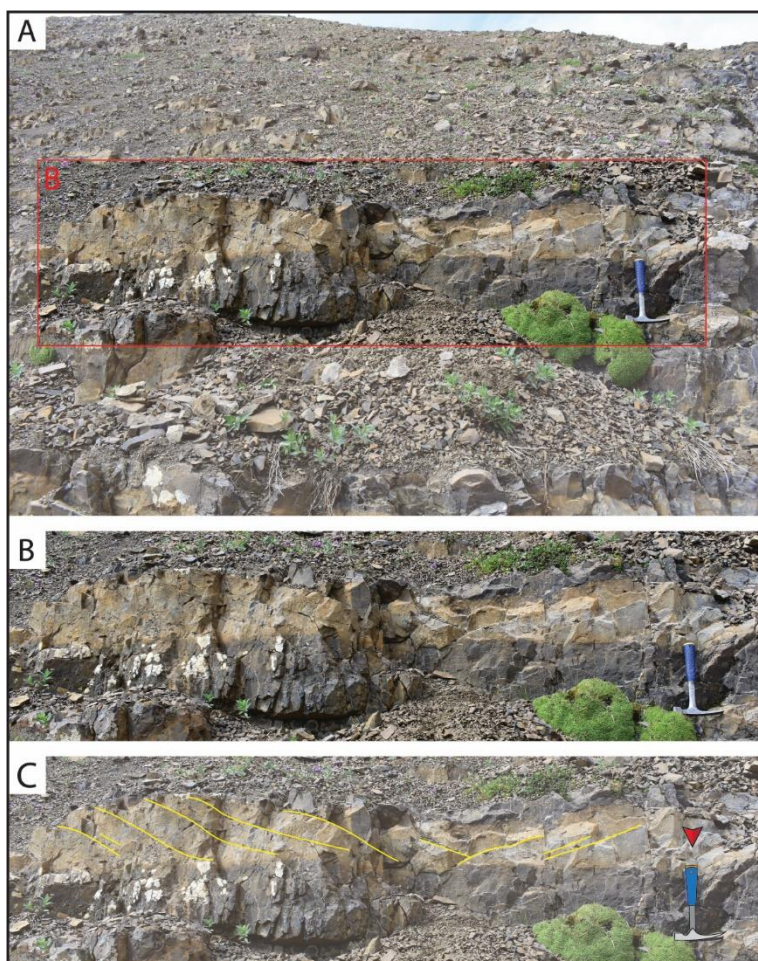
Figure 15: Sigmoidal features at 130.5 m. **A.** Outcrop with thick buff/grey coloured bed. Red box indicated area of interest. **B.** Sigmoidal features in bed (no annotations). **C.** Bed with sigmoidal features (yellow) with opposing directions that have a cross-cutting relationship. Geological hammer for scale.

59
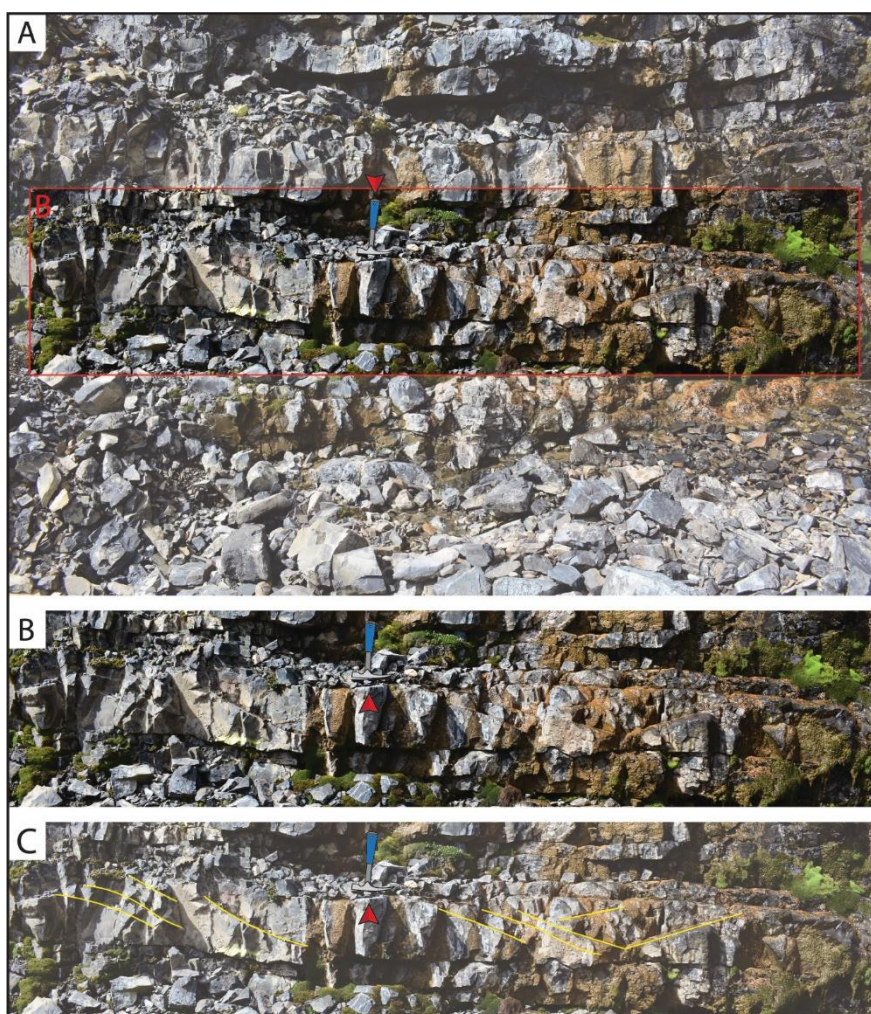
Figure 16: Sigmoidal features at 131 m. **A.** Outcrop with grey coloured bed. Red box indicated area of interest. **B.** Sigmoidal features in bed (no annotations). **C.** Bed with sigmoidal features (yellow) with opposing directions that have a cross-cutting relationship. Geological hammer for scale, marked with red arrow.
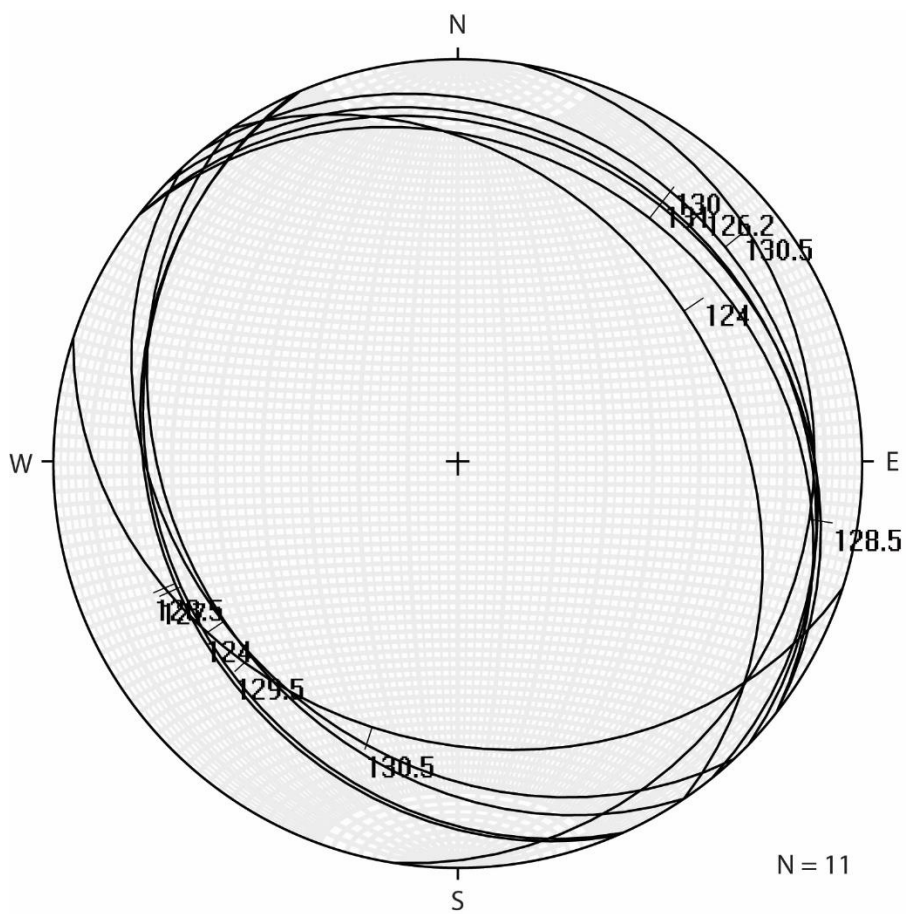
Figure 17: The orientation of the 11 measured sigmoidal features, after correction for the S0, show a bimodal distribution. Data is projected on a Lambert equal area stereonet.
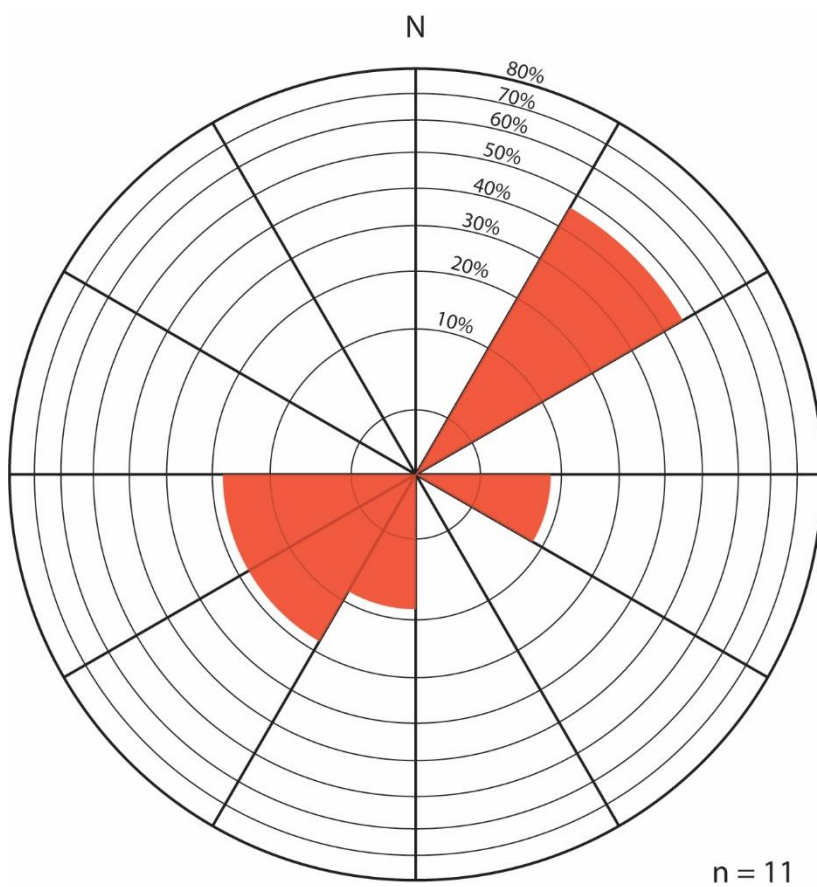
Figure 18: Paleoflow directions of the crossbedding in the upper member show a bimodal distribution towards the NE and SW (n = 11).
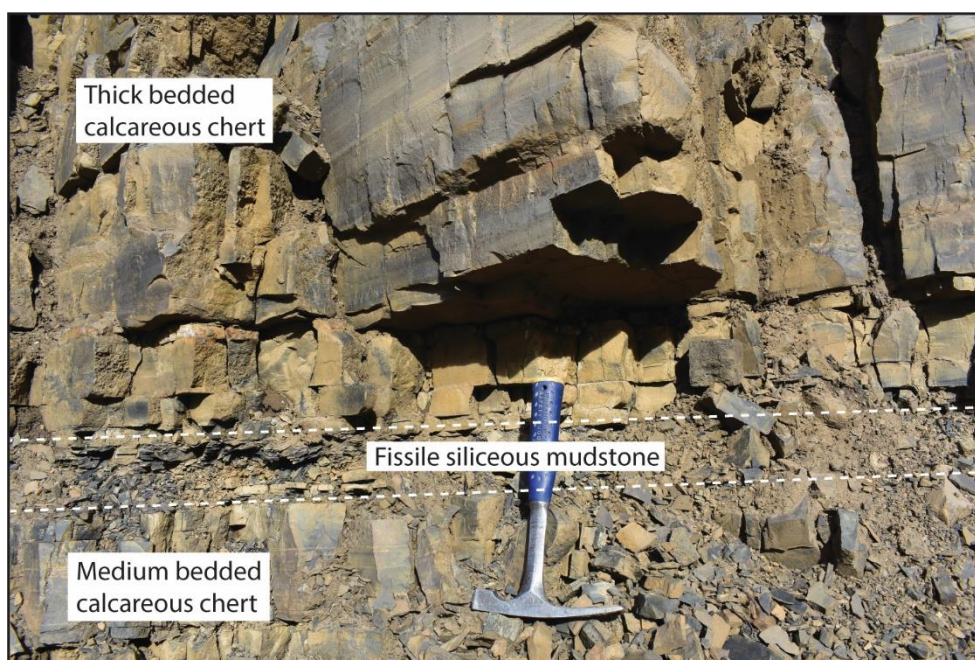
Figure 19: The slope forming succession contains alternating medium to thick calcareous chert beds and fissile siliceous mudstone. Geological hammer for scale.

Figure 20: In the upper half of the slope forming succession, every 1-10 m, thick beds occur with bigradational grading. **A.** Outcrop with prominent thick bed. **B.** Close up of bed. Grading is mimicked by colour, changing from buff to grey. Grading is indicated with light grey diamond. Geological hammer for scale.
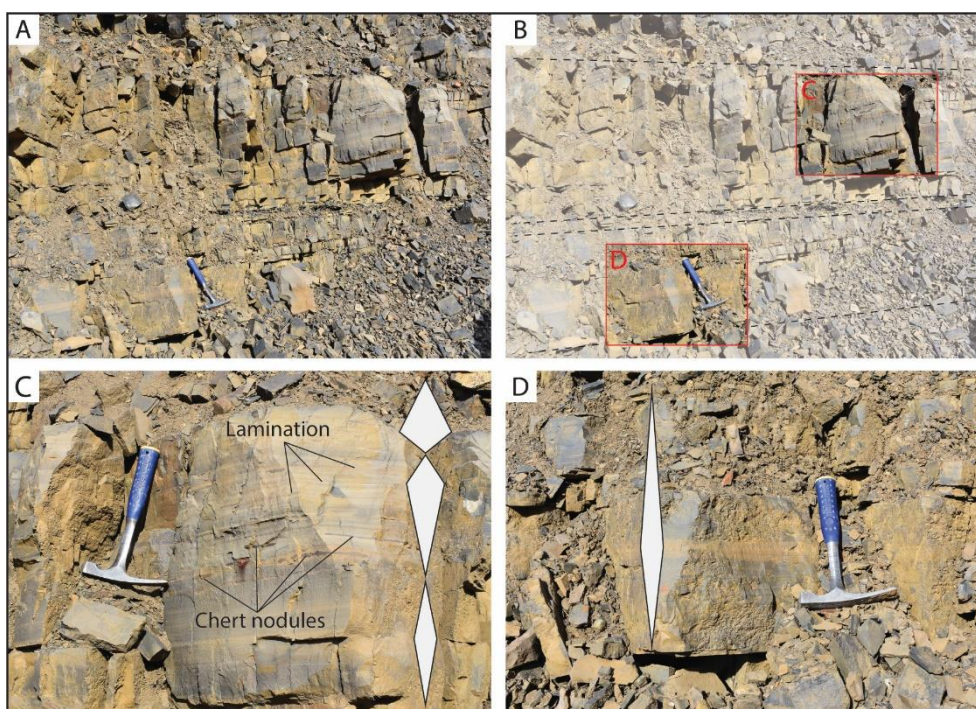
Figure 21: Bigradational grading is displayed on multiple scales. **A.** Outcrop with thick buff/grey-coloured beds. **B.** Red boxes mark areas of interest. Black dotted lines indicated bedding orientation. **C and D.** Beds contain thin parallel lamination, and chert nodules that are focused in horizons in the coarser parts of the bed. Grading is indicated with grey diamonds. Geological hammer for scale.
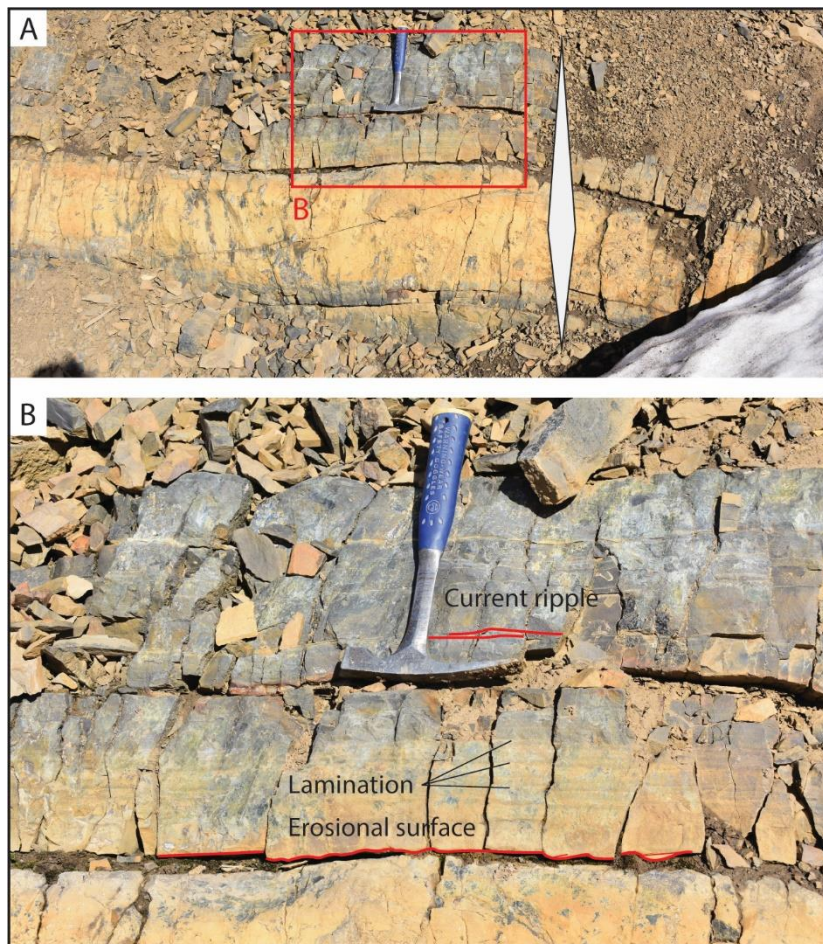
Figure 22: The bedding boundaries sometimes are undulated, resembling an erosional surface. Lamination and current ripples are present in the medium to thick beds. Grading is indicated with grey diamond. Geological hammer for scale.
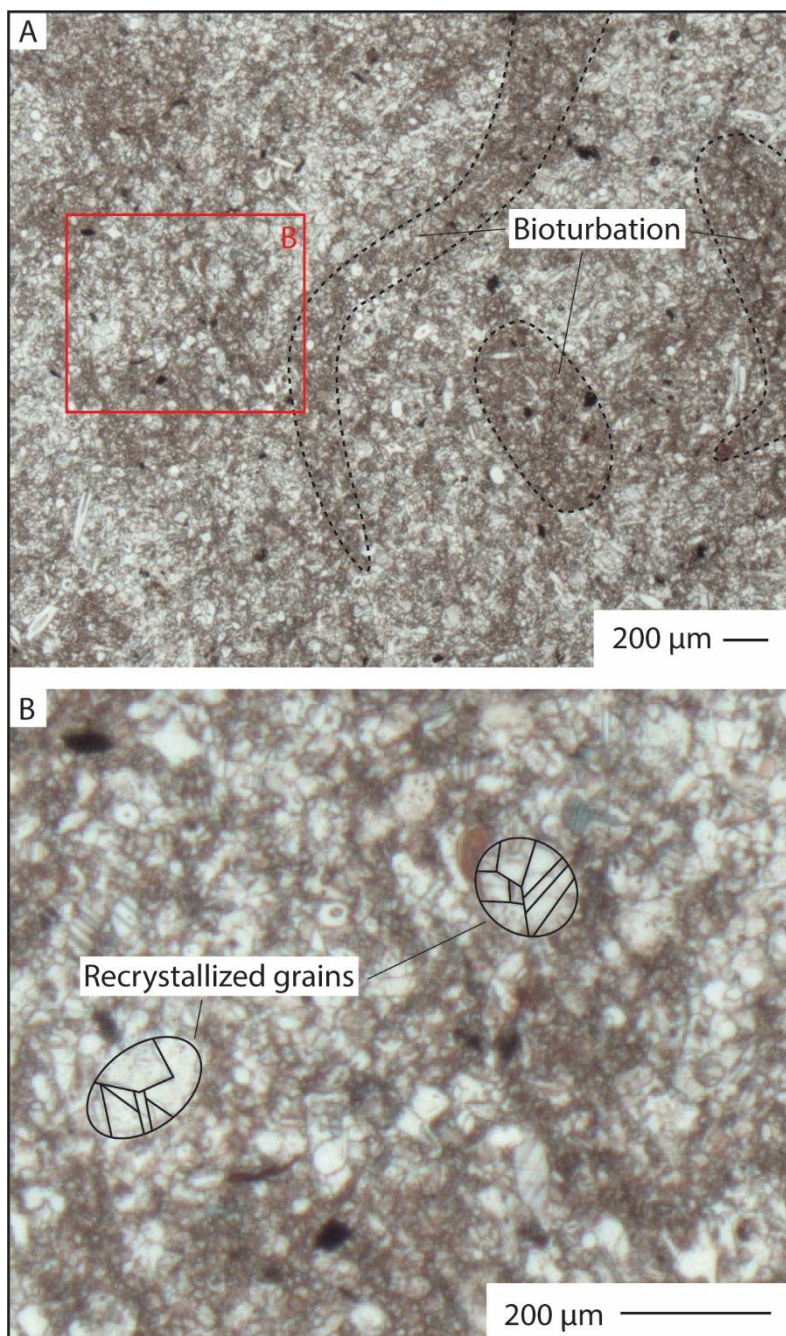
Figure 23: The micrograph from the thin section from the cross-bedding contains bioturbation (A). Grains are recrystallized (B). ImageJ recognizes individual sparite crystals as grains and underestimates the actual grain size.
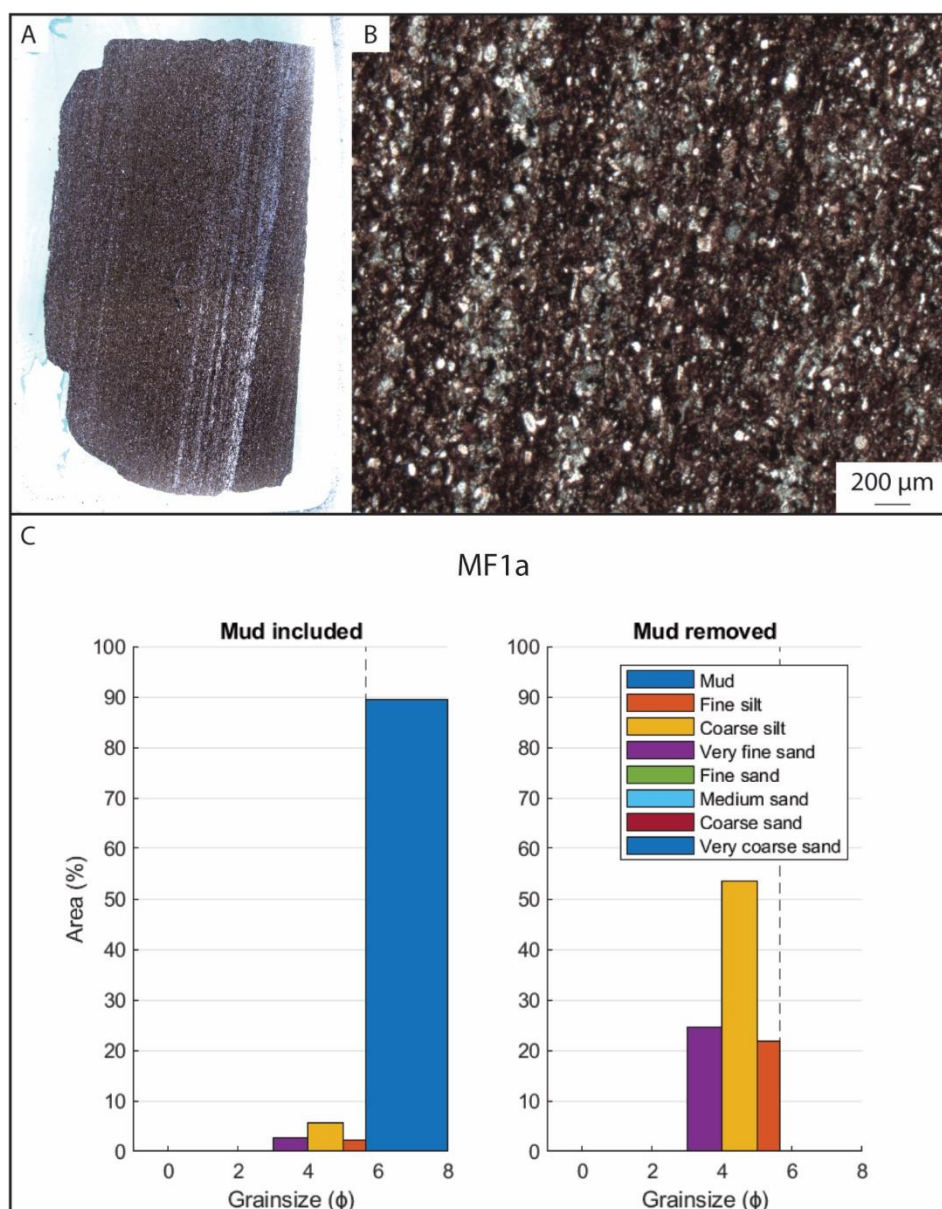
Figure 24: MF1a, Fine mudstone with basal silt laminae. Thin section (A), Micrograph (B), Grainsize distribution with and without matrix (C).
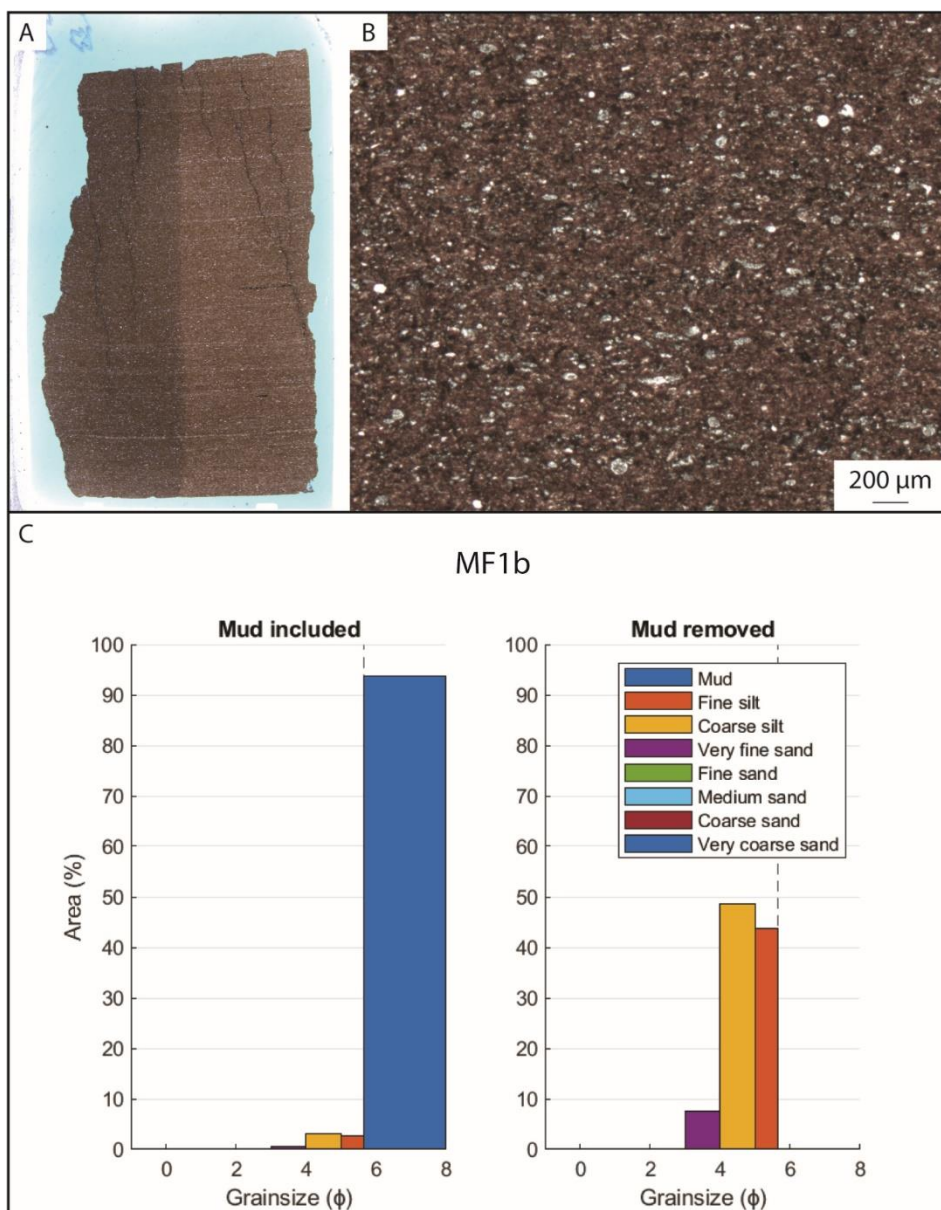
Figure 25: MF1b, Fine mudstone with parallel laminae. Thin section (A), Micrograph (B), Grainsize distribution with and without matrix (C)
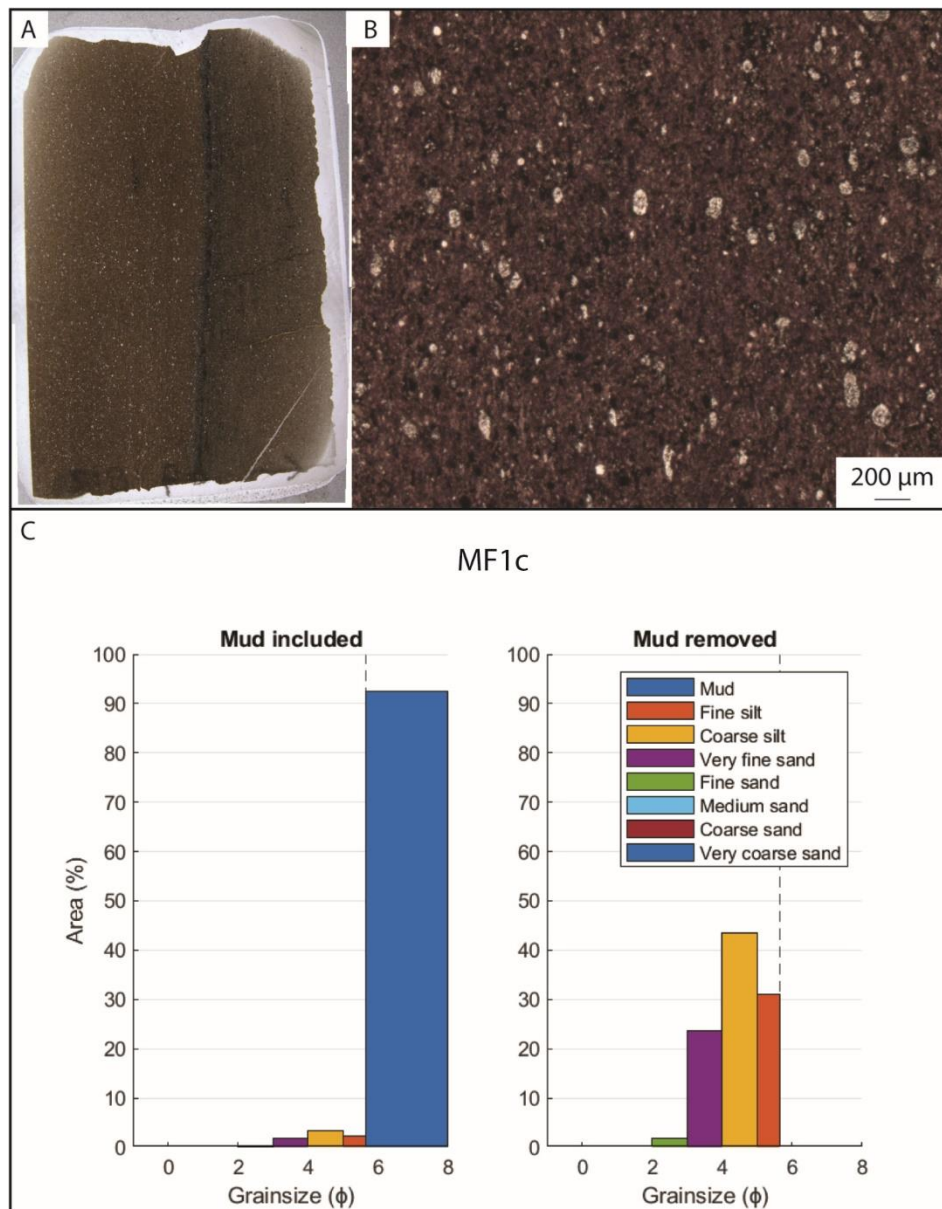
Figure 26: Burrowed fine mudstone. Thin section (A), Micrograph (B), Grainsize distribution with and without matrix (C)
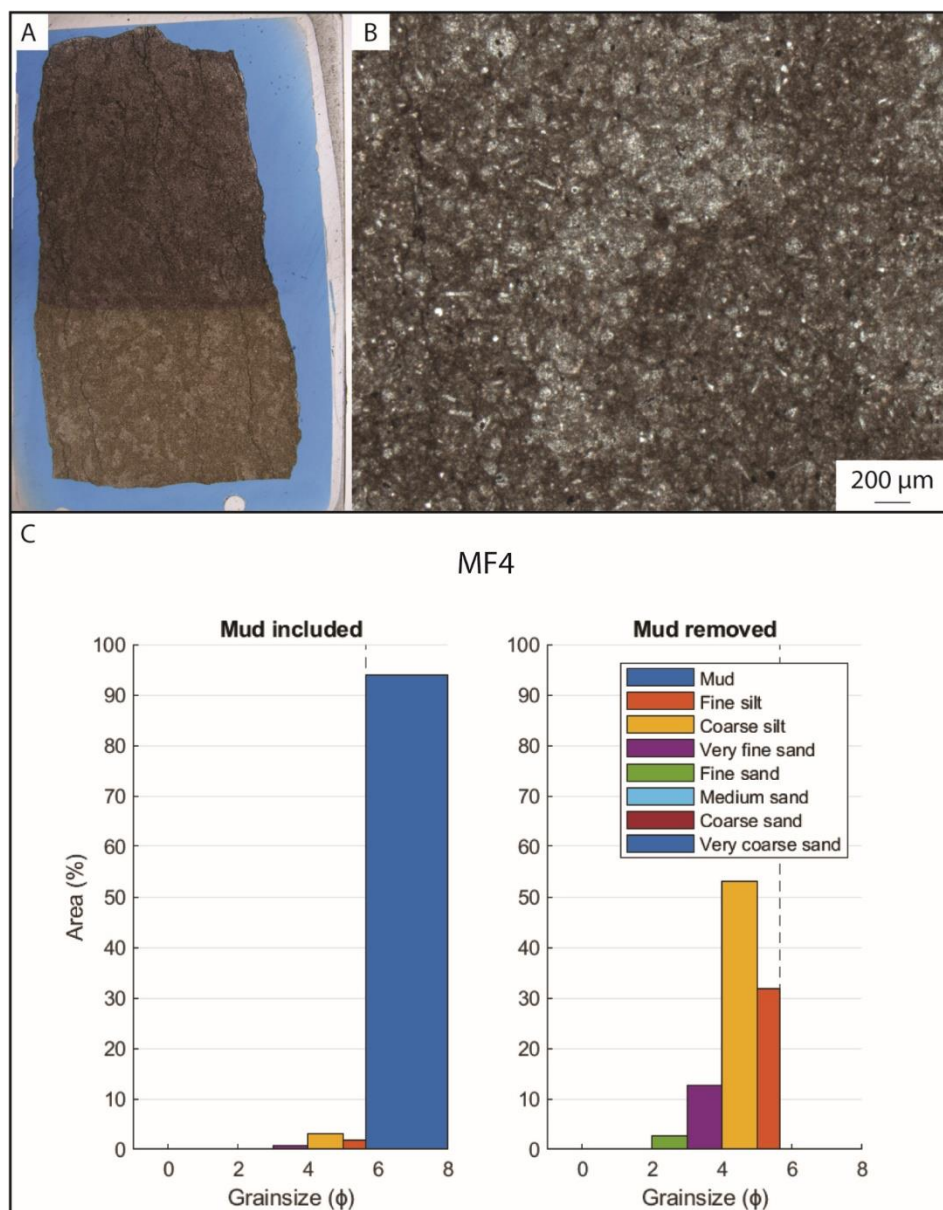
Figure 27: MF4, Calcisphere packstone. Thin section (A), Micrograph (B), Grainsize distribution with and without matrix (C)
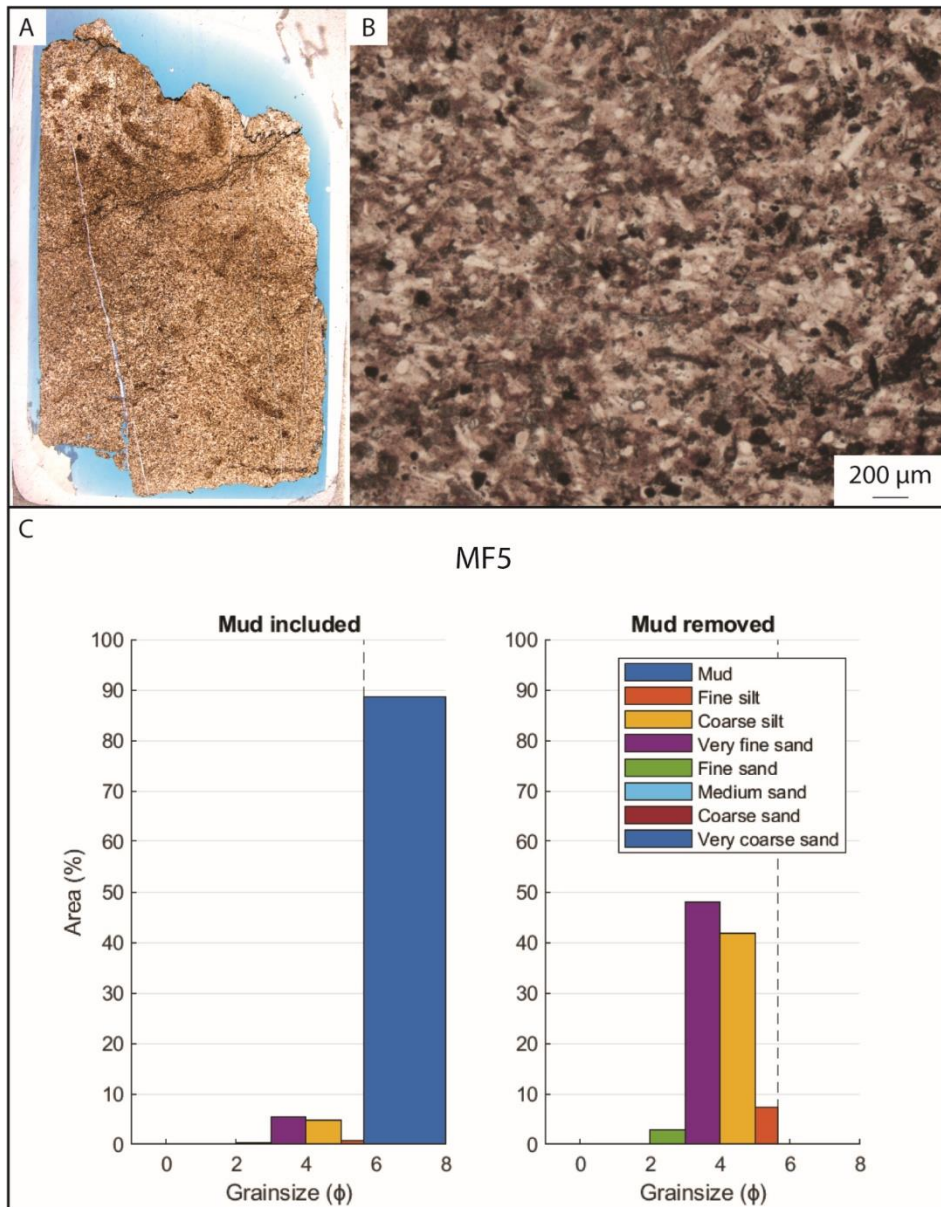
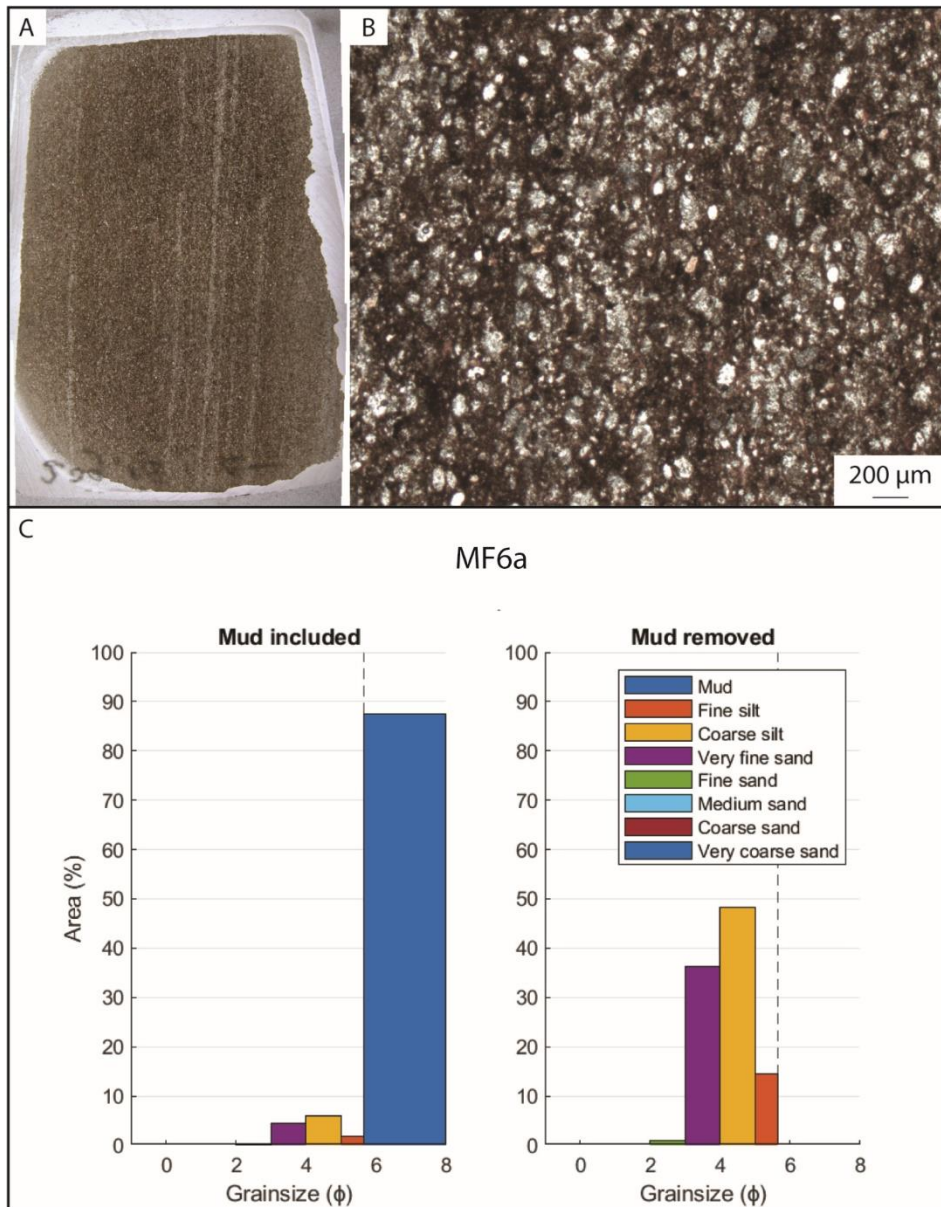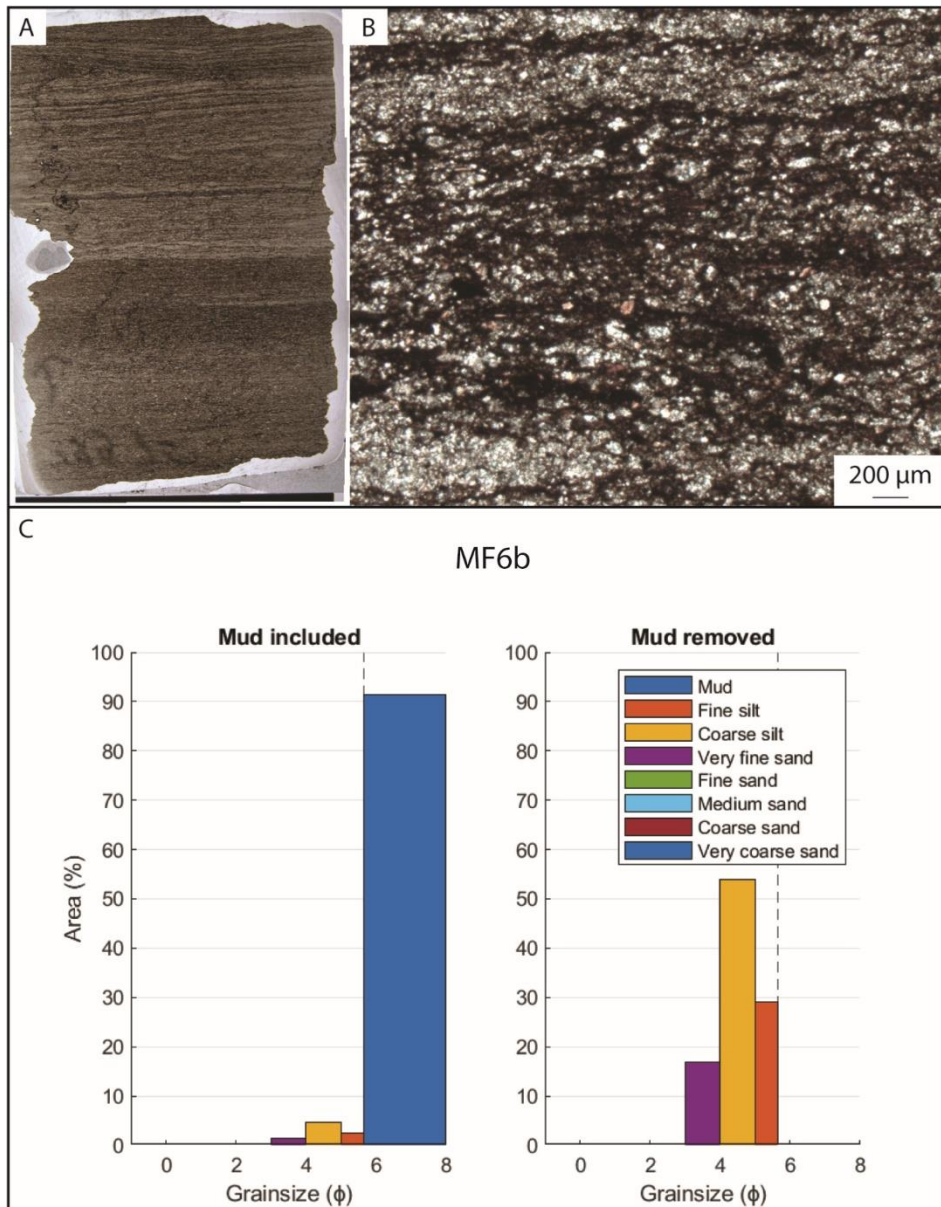Figure 28: MF5, Spiculitic sandy mudstone. Thin section (A), Micrograph (B), Grainsize distribution with and without matrix (C)

Figure 29: Laminated sandy mudstone. Thin section (A), Micrograph (B), Grainsize distribution with and without matrix (C)

Figure 30: Sandy mudstone with wavy laminae. Thin section (A), Micrograph (B), Grainsize distribution with and without matrix (C)
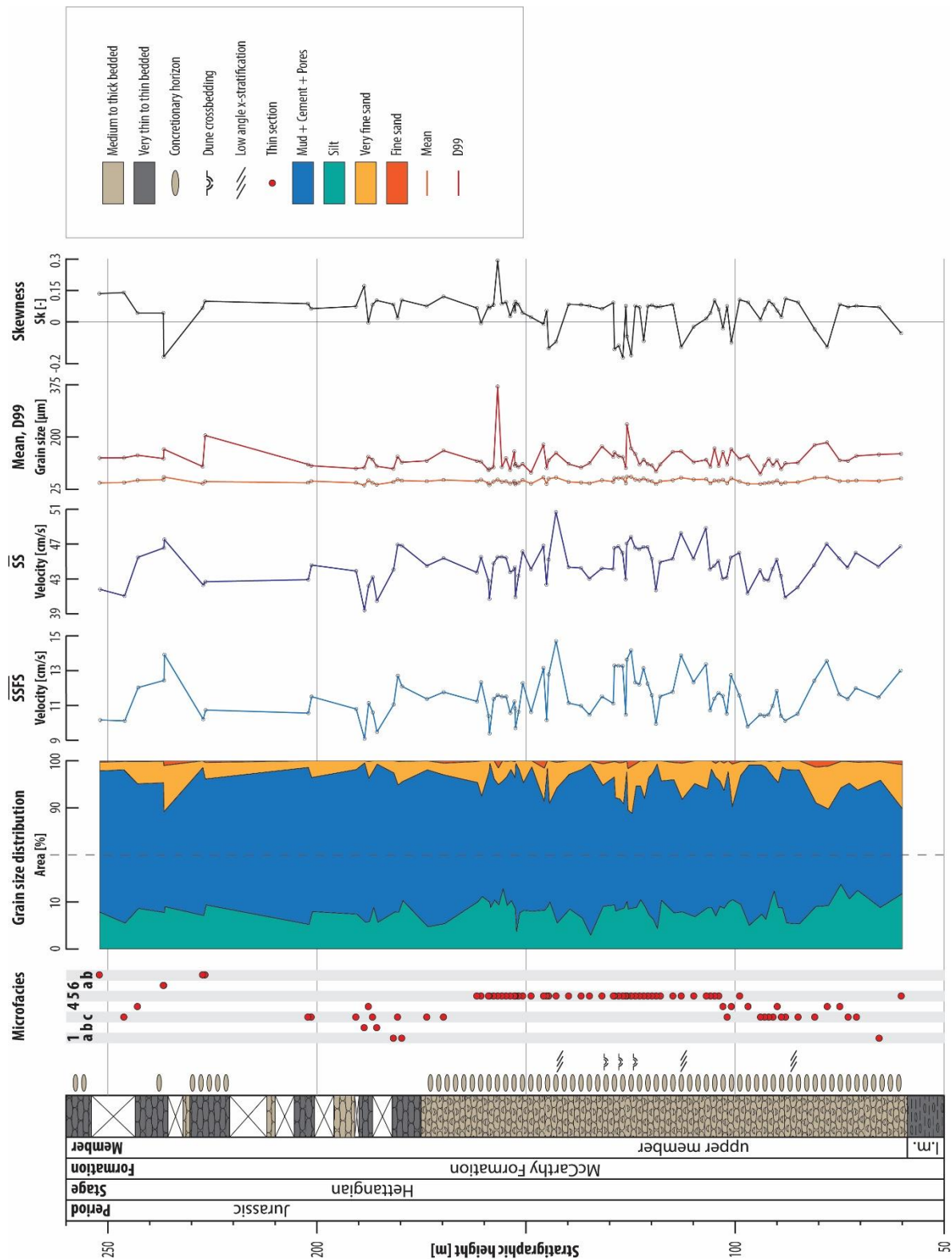
Figure 31: Stratigraphic log of the upper member from left to right: lithostratigraphy and microfacies distribution, modified from Veenma et al. (2022); Grain size distribution in area percentage obtained with ImageJ; Reconstructed paleocurrent velocity using the (modified) SSFS proxy by Wu et al. (2021) and the (modified) SS proxy by McCave et al. (2017); The mean and the D99, obtained with GRADISTAT (Blott and Pye, 2001) and a MATLAB function (supplementary materials) respectively; The skewness, obtained with GRADISTAT (Blott and Pye, 2001).
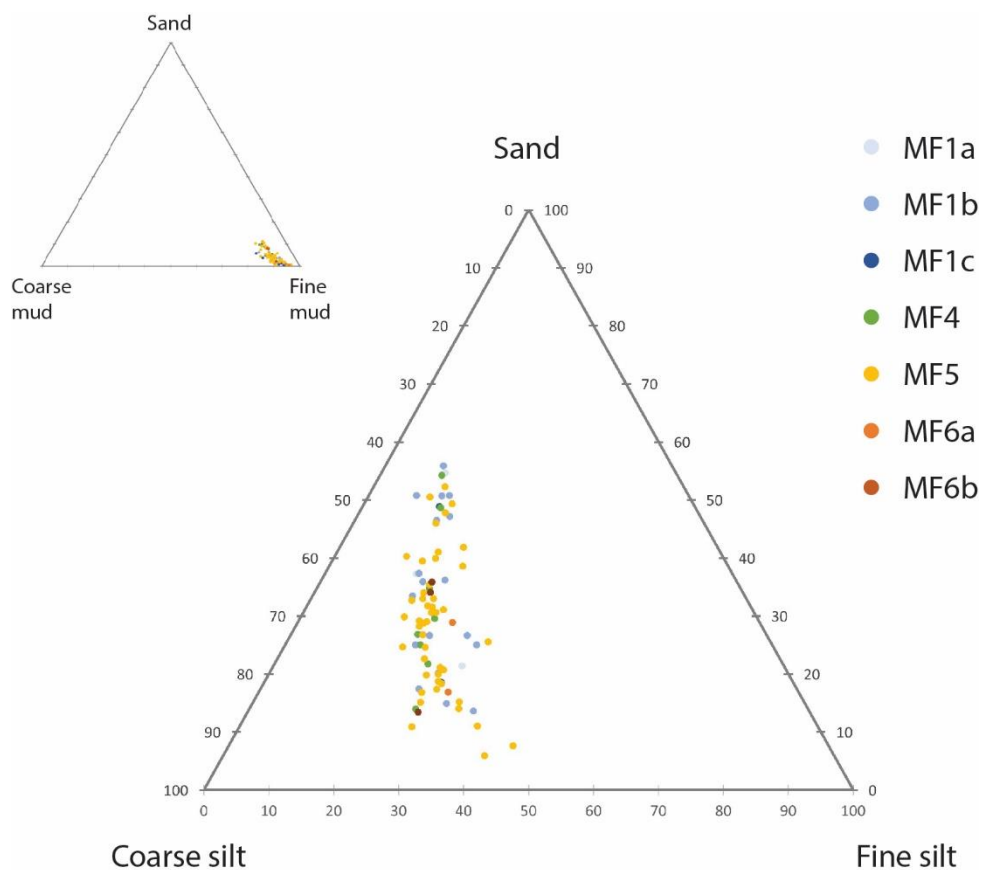
Figure 32: The texture of the samples, grouped by microfacies, summarized in two ternary diagrams. Top left has sand (62.5-500 μm), coarse mud (20-62.5 μm) and fine mud (0-20 μm) in the corners. Fine mud includes all matrix and is thus overestimated. Centre diagram has sand, coarse silt (31.25-62.5 μm) and fine silt (20-31.25 μm) in the corners. It shows distribution of the texture, normalized to exclude mud.
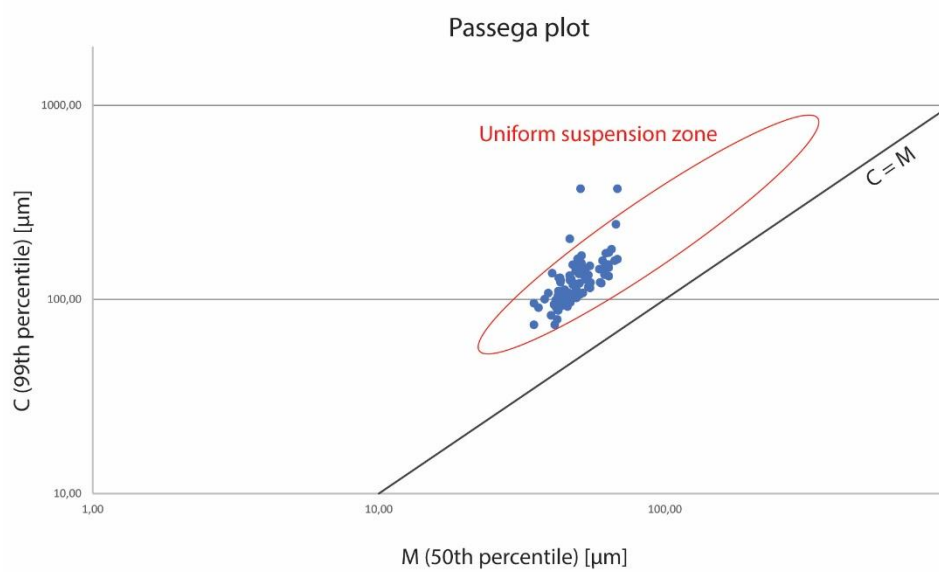
Figure 33: Samples plotted in a C/M diagram (Passega, 1964). The samples fall in the uniform suspension zone. The black line marks C=M. The blue dots mark the samples.
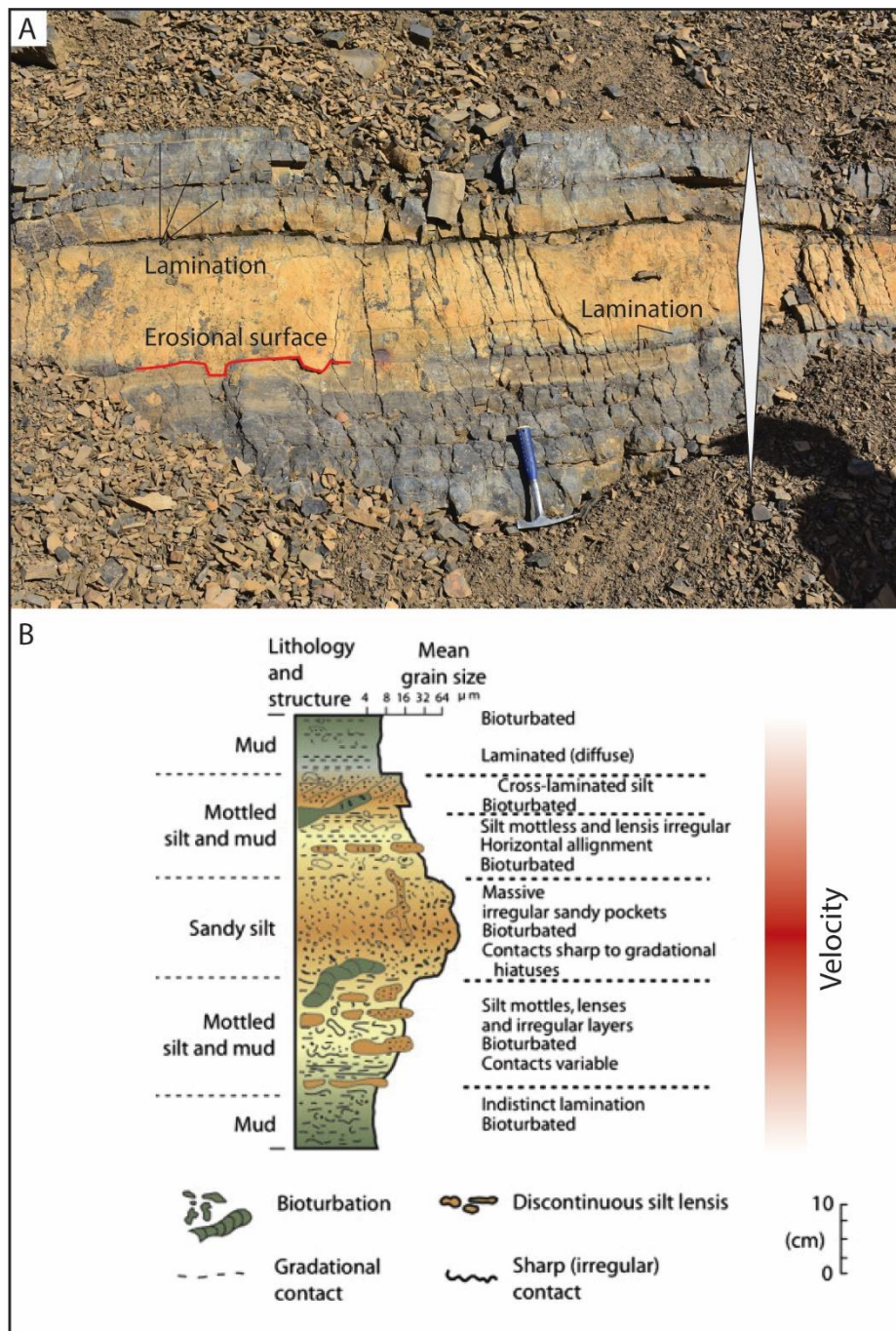
Figure 34: The bigradational bedding in the slope forming succession of the upper member is characteristic for contourite deposits. A: The bedding contains an erosive boundary at the level of highest inferred velocity. Above and below, the bed is laminated conform the facies model. Grading is indicated with grey diamond. Geological hammer for scale. B: Facies model (adapted from Rebesco et al. 2014).